

NRL/MR/6720--95-7659

Systematic Analysis of Saturn Wire Array Implosion Observations

P. E. PULSIFER
J. P. APRUZESE
K. G. WHITNEY

*Radiation Hydrodynamics Branch
Plasma Physics Division*

R. B. SPIELMAN
T. J. NASH
J. S. MCGURN
L. E. RUGGLES

*Sandia National Laboratories
Albuquerque, NM*

April 19, 1995

19950414 125

Approved for public release; distribution unlimited.

REPORT DOCUMENTATION PAGE

Form Approved
OMB No. 0704-0188

Public reporting burden for this collection of information is estimated to average 1 hour per response, including the time for reviewing instructions, searching existing data sources, gathering and maintaining the data needed, and completing and reviewing the collection of information. Send comments regarding this burden estimate or any other aspect of this collection of information, including suggestions for reducing this burden, to Washington Headquarters Services, Directorate for Information Operations and Reports, 1215 Jefferson Davis Highway, Suite 1204, Arlington, VA 22202-4302, and to the Office of Management and Budget, Paperwork Reduction Project (0704-0188), Washington, DC 20503.

1. AGENCY USE ONLY (Leave Blank)		2. REPORT DATE April 20, 1995		3. REPORT TYPE AND DATES COVERED	
4. TITLE AND SUBTITLE Systematic Analysis of Saturn Wire Array Implosion Observations				5. FUNDING NUMBERS	
6. AUTHOR(S) P.E. Pulsifer, J.P. Apruzese, K.G. Whitney, R.B. Spielman,* T.J. Nash,* J.S. McGurn,* and L.E. Ruggles*					
7. PERFORMING ORGANIZATION NAME(S) AND ADDRESS(ES) Naval Research Laboratory Washington, DC 20375-5320				8. PERFORMING ORGANIZATION REPORT NUMBER NRL/MR/6720--95-7659	
9. SPONSORING/MONITORING AGENCY NAME(S) AND ADDRESS(ES) Defense Nuclear Agency 6801 Telegraph Road Alexandria, VA 22310-3398				10. SPONSORING/MONITORING AGENCY REPORT NUMBER	
11. SUPPLEMENTARY NOTES *Sandia National Laboratories Albuquerque, NM 87115					
12a. DISTRIBUTION/AVAILABILITY STATEMENT Approved for public release; distribution unlimited.				12b. DISTRIBUTION CODE	
13. ABSTRACT (Maximum 200 words) A comprehensive analysis is presented of data from a series of aluminum wire-array implosions conducted two years ago on the Saturn generator at Sandia National Laboratories. These experiments were originally designed to explore how results from Physics International's Double Eagle facility would scale to larger masses and implosion velocities. Parameters varied imploding mass and maximum implosion velocity, holding total kinetic energy constant. Data include filtered XRD traces, time-integrated keV spectra, and K-shell pinhole photographs, from which we infer mean radiated power, kinetic energy at stagnation, plasma temperature and density, and average fraction of imploding mass participating in keV radiation. The introduction of electronic data analysis for all quantities except pulsewidth makes the procedure both rapid and self-consistent. The derived quantities show systematic trends, some correlating with yield behavior. As expected, the particle kinetic energy maximizing yield was a small multiple of the atomic number-dependent energy needed to ionize and sufficiently heat the plasma. The mass participation fraction, which showed considerable variation, correlated positively with 1 keV yield. The procedures described allow efficient and meaningful analysis of PRS experiments. The results have implications for high-yield wire-array implosion designs, especially with high-power, short-pulse accelerators.					
14. SUBJECT TERMS X-ray data analysis Wire implosions z-pinch PRS yield				15. NUMBER OF PAGES 43	
				16. PRICE CODE	
17. SECURITY CLASSIFICATION OF REPORT UNCLASSIFIED	18. SECURITY CLASSIFICATION OF THIS PAGE UNCLASSIFIED	19. SECURITY CLASSIFICATION OF ABSTRACT UNCLASSIFIED	20. LIMITATION OF ABSTRACT UL		

CONTENTS

1. Introduction	1
2. Simple implosion model	2
3. Pulsewidth analysis	4
4. Spectral analysis	5
5. Pinhole photograph analysis	7
6. Results	9
7. Conclusions	11
8. References	12
9. Figures	13

Accession For	
NTIS CRA&I	<input checked="" type="checkbox"/>
DTIC TAB	<input type="checkbox"/>
Unannounced	<input type="checkbox"/>
Justification	
By	
Distribution/	
Availability Codes	
Dist	Avail and/or Control
A-1	

SYSTEMATIC ANALYSIS OF SATURN WIRE ARRAY IMPLOSION OBSERVATIONS

Introduction

In this report, we will describe the analysis of data from a set of aluminum wire-array implosions conducted on the Saturn accelerator at Sandia National Laboratories.^{1,2} The Saturn experiments were conducted to explore the validity of theoretical implosion models by investigating the variation of the keV x-ray yield as a tradeoff is made between the amount of mass imploded and the maximum velocity achieved in the implosion. In this series of experimental shots, the array mass per unit length m and the initial array radius r_0 were varied in a way designed to keep the total kinetic energy in the implosion roughly constant. Thus, variations in radiative yield should reflect only how efficiently this kinetic energy is converted to keV radiation.

In the experiments, both total and keV radiative yield showed a discernible trend as a function of either array mass or initial radius. One goal of the present analysis was to explain this trend by gaining greater understanding of the average plasma conditions during the implosion. Two important factors which predict output power in the present experiments are the average ion kinetic energy at stagnation and the fraction of the imploding mass involved in the radiation.

The importance to K-shell radiation of having the proper ion kinetic energy at stagnation has become well recognized.³ This energy must be large enough but not too large: The implosion must ionize the imploding mass and heat the electrons sufficiently to radiate, but should not cause other processes (stripping, runaway generation) to dominate. This theory is well supported in the present experiments.

The degree of mass participation in the radiation also strongly influences the keV output.² In the present experiments, we found considerable variation from shot to shot in the fraction of the imploding mass involved in K-shell radiation (from 0.04% to 78%). These values correlated well with the K-shell radiative power.

Experimental observations from the runs consisted of

1. Filtered PCD output records as a function of time;
2. Time-integrated keV spectra;
3. Pinhole photographs, both time-integrated and at time intervals.

The systematic analysis given here uses a procedure developed earlier at NRL.⁴ Using this procedure, we can infer from x-ray photodiode, spectroscopic and pinhole measurements the average radiated power, the average ion density and plasma temperature, and the average fraction of total mass that was involved in K shell x-ray radiation.

This report is organized as follows. First, a simple implosion model is presented, to introduce the terminology and basic scaling behavior. Parameters for the experimental runs are presented. Next, the details are given for analysis of the pulsewidth, line spectrum, and pinhole photograph data. The measurements from the data are then summarized and trends are pointed out.

Simple implosion model

The slug model gives a good basic framework for discussion of the implosion dynamics. In this model,⁵ all of the imploding material forms a cylindrically symmetric shell at a radius r , which obeys the force equation

$$m \frac{d^2 r}{dt^2} = \frac{1}{2\ell} \frac{\partial L}{\partial r} I^2 \quad (1)$$

where m is the mass per unit length, ℓ is the wire length, $I(t)$ is the total current, and $L(t)$ is the inductance of the circuit element consisting of the imploding material and the concentric, external anode. For an array of N wires,

$$\frac{\partial L}{\partial r} = -\frac{N-1}{N} \frac{\mu_0}{2\pi} \frac{\ell}{r} \equiv -\frac{L_0}{r} \quad (2)$$

where $\mu_0 = 4\pi \times 10^{-7} \text{ H m}^{-1}$.

The current through the pinch at a given time is determined by the parameters of the transmission line circuit, which has a total inductance L_T and impedance Z_0 . The circuit equation is:

$$\frac{dL_T I}{dt} + I Z_0 = V(t) \quad (3)$$

The simultaneous solution of Eq. (1) and Eq. (3) for a given voltage waveform $V(t)$ gives the radial position and velocity of the implosion, as long as plasma pressure is negligible.

In designing the parameters for the experiments described here, both the force and circuit equations were solved for an input $V(t)$ appropriate for Saturn. Useful insight, however, can also be gained by neglecting the circuit equation and assuming a simplified linear time dependence for the current:³

$$I(t) = I_1 t. \quad (4)$$

To aid in the description of the experimental results, we will summarize results obtained earlier³ for the solution of Eq. (1) with $I(t)$ from Eq. (4).

First, we write Eq. (1) in dimensionless form, by defining

$$x \equiv r/r_0; \quad \tau \equiv t/t_0; \quad i \equiv I/I_0 \quad (5)$$

where r_0 is the initial array radius, and the constants t_0 and I_0 are left arbitrary for now. The dimensionless form of Eq. (1) is

$$x \frac{d^2 x}{d\tau^2} = -A i^2 \quad (6)$$

with

$$A \equiv \frac{\frac{1}{2}(L_0/\ell)I_0^2}{m(r_0/t_0)^2}. \quad (7)$$

Because of Eq. (4), current and time are in one-to-one correspondence. We can combine these by defining

$$q = [A^{1/4}(I_1 t_0 / I_0)^{1/2}] \tau \quad (8)$$

so that Eq. (6) becomes

$$x \frac{d^2 x}{dq^2} = -q^2, \quad (9)$$

with the boundary conditions $x(0) = 1$ and $q(0) = 0$.

Eq. (9) can be numerically solved to give a curve of $x(q)$, which is the general radial trajectory of the slug-model implosion with a linear current rise. This solution and that for dx/dq are shown in Fig. (1). The actual radial values are given by $r = r_0 x(q(t))$, with the appropriate conversion factors:

$$q(t) = \left[\frac{\frac{1}{2}(L_0/\ell)I_1^2}{m r_0^2} \right]^{1/4} t \quad (10)$$

Note that this relation is independent of the choice of the normalization constants I_0 and t_0 , which have not yet been defined. Characteristic values that might be used for normalization are the maximum current $I_{max} = I_1 t_{max}$ and the circuit relaxation time $t_{LR} = L_0/Z_0$.

In this model, all implosions behave in the same way, following the curve in Fig. (1) from $x(0) = 1$ to stagnation at $x(q_f) = x_f$. Stagnation occurs at the point where the plasma pressure, omitted from Eq. (1), exceeds the inward magnetic pressure. We assume that this pressure becomes important too suddenly to affect the overall dynamics (i.e., the zero-pressure curve $x(q)$), and arbitrarily define the stagnation position x_f based on experimental observations. The usual definition has been³ for $0.1 \leq x_f \leq 0.2$; this choice is supported by the pinhole photograph data presented here. The stagnation time t_f is derived from q_f by using Eq. (10). The stagnation point is also the time of maximum implosion velocity (proportional to dx/dq).

An important implosion parameter is the kinetic energy per ion³ $K_i \equiv \frac{1}{2} m_i v_f^2$, where m_i is the ion mass and v_f is the ion velocity at the stagnation time t_f . This can be written as

$$K_i = \mu_i \left[q_f \left(\frac{dx}{dq} \right)_f \right]^2 (r_0/t_f)^2 \quad (11)$$

where the energy conversion factor $\mu_i = 1.398 \times 10^7 \text{ eV cm}^{-1} \text{ ns}$. For efficient K-shell emission, K_i must exceed an energy E_{min} , which is required to strip all but one or two electrons from the atom and heat the stripped electrons sufficiently to radiate. For aluminum, E_{min} is roughly 12 keV/ion.^{1,3} The parameter

$$\eta = K_i / E_{min} \quad (12)$$

indicates the degree to which the minimum-energy condition is fulfilled. We expect that K-shell radiation will be greatest when $\eta > 1$ but not for $\eta \gg 1$, when processes other than K-shell radiation will dominate.

The energy parameter determining the maximum total radiation is the kinetic energy per unit length³ $K_c = \frac{1}{2}mv_f^2$, which is given by

$$K_c = \frac{1}{4}(L_0/\ell)I_{max}^2 \left[\frac{1}{q_f} \left(\frac{dx}{dq} \right)_f \right]^2. \quad (13)$$

We expect that the total x-ray yield will increase as K_c is increased (though K_c was held constant in the experiments analyzed here).

The machine parameters affecting the implosion are mass m , initial radius r_0 and current rise rate I_1 (or maximum current $I_{max} = I_1 t_f$). Since q_f and $(dx/dq)_f$ are the same for all implosions, the following scaling must apply for the implosion time, particle energy (for a given element), and total energy:

$$t_f \sim [mr_0^2]^{1/2}/I_{max} \quad (14a)$$

$$\eta \sim m^{-1}I_{max}^2 \quad (14b)$$

$$K_c \sim I_{max}^2. \quad (14c)$$

The η value is independent of r_0 and K_c is independent of both m and r_0 .

The shot parameters for the two experimental series are given in Table I. Two sets of 6 shots were made, one set using larger initial radii (and anode diameter) than the other. The implosion time for these shots varies from about 50 ns at low mass to 90 ns at high mass, based on the linearly rising current model; with the Saturn circuit model, these times would be slightly shorter.

The accuracy of the simple model in determining implosion energy can be assessed by comparing the tabulated values of the energy parameter η , obtained using the more accurate Saturn circuit model (Eq. (3)), and of $\eta_{0.2}$, the same parameter computed from the linear current model with $x_f = 0.2$. The difference is generally under 10%. The experimental design of holding K_c constant is reflected in the invariance of the product $m\eta = 2 \times 10^3$. The successful achievement of this goal can be seen in the near constancy of the maximum current I_{max} .

Pulsewidth analysis

The pulsewidth was evaluated from the net keV and total radiation observations. Output traces from the filtered x-ray PCD's, which had a resolution of better than 10 ns, are shown in Fig. (2). The pulsewidth was defined to be the full width at half-maximum, which quantity was uniquely given in the present data. Note, however, that two pulses were often present, a strong initial pulse and decay followed by a "bounce" pulse. The bounce is prominent in the high-mass shot 1498 and is present in all of the large initial radius shots (set 2, Fig. (2b)). In these observations, however, the half-maximum width never extended beyond the first (and stronger) peak.

Table I. Shot parameters

Shot No.	Array dia (cm)	Mass ($\mu\text{g/cm}$)	I_{max} (MA)	Total yield (kJ)	keV yield (kJ)	$\eta_{0.2}$	η
<i>Set 1: Anode diameter 2.80 cm</i>							
1483	1.71	328	8.9	224	76.0	6.9	6.0
1484	1.59	473	8.7	242	38.1	5.7	4.2
1487	1.46	739	9.0	291	30.0	3.1	2.7
1488	1.40	949	9.4	224	20.0	2.7	2.2
1489	1.34	1313	8.8	270	13.2	1.8	1.6
1498	1.28	2052	9.8	228	4.9	1.3	0.95
<i>Set 2: Anode diameter 4.80 cm</i>							
1492	3.04	118	9.1	172	8.0	20	22
1493	2.81	161	9.6	170	12.2	16	17
1494	2.73	185	9.4	196	22.4	14	15
1495	2.42	328	9.7	331	63.3	8.2	8.3
1496	2.29	473	9.7	364	61.2	5.7	5.6
1497	2.20	739	9.9	338	30.1	3.8	3.5

Results for the keV pulsewidth are plotted in Fig. (3), as a function of both array radius and mass. While the data show some variability, generally the pulsewidth increases with mass and decreases with increasing initial radius. The qualitative differences in the output traces of Fig. (2a) and Fig. (2b) will also be reflected in the pinhole data presented below, with broader, more irregular output traces associated with diffuser, lower-contrast pinhole images.

Spectral analysis

The time-integrated x-ray spectra of the two sets of Saturn shots are shown in Fig. (4). The important K-shell lines are listed in Table II. These lines can be clearly seen in the spectra of almost all the experimental shots. While spectral broadening and properties of satellite lines could in principle be used to obtain information on plasma conditions, experimental conditions dictate the line energy as the most reliable spectral diagnostic. Peak widths depend on the time-varying and parameter-dependent width of the source, and so provide no readily obtainable information on plasma parameters. The actual power emitted in a single line, given by the integral under the spectral curve, cannot be determined with certainty because of the difficulty of calibrating the instrumentation, and of accurately determining continuum radiation. The ratio between power emitted in different lines, however, is independent of instrumental calibration, and is a sensitive function of plasma density and temperature. We use the ratio of the most prominent lines, the Ly α and He α lines, in our analysis.

The energy radiated in each line was found by computer analyzing the digitized spectra. The

Table II. Energies of important Al K-shell lines and edges

Line	Energy (eV)	Wavelength (Å)
He IC	1588	7.81
He α	1598	7.76
Ly α	1728	7.17
He β	1869	6.64
He γ	1964	6.31
He δ	2006	6.18
He edge	2086	5.94
Ly β	2048	6.05
Ly γ	2160	5.74
Ly δ	2212	5.61
H edge	2304	5.38

strategy used was as follows. To minimize interference from data jitter, we analyzed not the spectrum itself, but its integral. These integrals are shown in Fig. (5), and are sized so they may be overlaid onto the corresponding spectra of Fig. (4). Clearly, a spectral line causes a sudden increase in the slope of the integral curve. The energy radiated in the line is the increase along the ordinate of the integrated curve from where its slope sharply increases to where its slope levels off. The magnitude of the slope of the integrated curve outside the spectral lines is proportional to the baseline height of the spectrum, or to the amount of continuum radiation at a given energy. For the present analysis, no attempt was made to subtract such "background" radiation from the total line energy.

To identify spectrum peaks, the "average" or baseline slope of the integral curve was computed as the slope between the initial point and the current point. This was compared to the "current" slope (average of slope at next 2 pts). A peak was deemed to begin whenever

$$(\text{current slope}) > \epsilon_0 * (\text{baseline slope}), \quad (15)$$

where $\epsilon_0 \approx 2$ is a convenient factor, whose exact value is not important for the sharp peaks found here. Two strategies were tried for numerically defining the end of the peak:

$$1. \quad (\text{current slope}) < \epsilon_1 * (\text{baseline slope}) \quad (16a)$$

$$2. \quad (\text{current slope}) < (\text{max slope during peak})/\epsilon_1 \quad (16b)$$

where $\epsilon_1 \approx 2$ is another arbitrary factor chosen for numerical convenience. The criterion in Eq. (16a) combines sub-peaks, and is insensitive to forked peaks or satellites. Thus, if the continuum signal increases on the high-energy side line peak (typically so at the high-energy end of spectrum), this criterion tends to miss the end of that peak and so group all peaks in the tail together. The criterion

in Eq. (16b) sensitively resolves almost all peaks, but may be too sensitive when there is jitter in the data. The first strategy was used for the present results.

Some results from the spectroscopic analysis are shown in Table III. The range of photon energies between 1.5 keV and 2.5 keV was used in the analysis; this range was of primary interest and was also where the instruments were most accurate. This energy range typically included 50–60% of the total energy in the obtained spectra; the fraction for each shot is given in the second column of the table. The third column shows the fraction of the total energy in the restricted range that was emitted in line radiation. Later columns show the fraction of the total restricted energy that was emitted in each of the lines whose energies are listed in Table II; these should sum roughly to the total in the third column. Line satellites are generally included with the line totals. Line ratios are found by simply taking the ratio of the column figures for the desired lines; for the present analysis, we used the ratio of Ly α to He α (+ intercombination) lines, since these were always the most prominent.

Table III. Fraction of keV radiated energy in atomic lines

Shot No.	Fraction in 1.5–2.5 keV	Fraction of restricted spectrum energy								
		Lines	He α	Ly α	He β	He γ	He δ	Ly β	Ly γ	Ly δ
1483	0.719	0.618	0.164	0.242	0.035	0.017	0.017	0.092	0.024	0.015
1484	0.466	0.593	0.202	0.253	0.034	0.017	0.017	0.028	0.013	0.009
1487	0.677	0.614	0.199	0.276	0.034	0.016	0.018	0.028	0.015	0.009
1488	0.669	0.647	0.226	0.298	0.031	0.016	0.013	0.028	0.013	0.006
1489	0.664	0.666	0.241	0.306	0.033	0.015	0.014	0.026	0.012	0.005
1492	0.106	0.709	0.291	0.357	0.056					
1493	1.000	0.560	0.188	0.238	0.034	0.011	0.006	0.053	0.018	0.007
1494	0.644	0.821	0.238	0.375	0.050	0.016	0.017	0.079	0.028	0.011
1495	0.006	0.522	0.187	0.256	0.038	0.017	0.018			
1496	0.555	0.547	0.200	0.211	0.027	0.016	0.016	0.031	0.016	0.009
1497	0.517	0.543	0.232	0.232	0.035	0.017	0.015			
1498	0.603	0.712	0.269	0.338	0.028	0.012	0.008	0.023	0.010	0.003

Pinhole photograph analysis

The main goal in analysis of the time-integrated pinhole data was to determine the width of the keV radiating region. Two time-integrated photographs were taken, one high-gain and one low-gain, as well as 10 fixed-time snapshots, taken at intervals of 3 ns for a 1 ns exposure time. Data acquisition was electronic, and corrections were made for the detector response before data analysis was begun.

The high-gain, time-integrated photograph was used for the present analysis. This image was entered into the computer, and an algorithm was developed to obtain an average value of the pinch width that correlated well with visual observation, even for irregular implosions and faint images. No densitometry-type calibration was made, because the degree of arbitrariness inherent in the determination of pinch radius for any one shot made such precision unnecessary. However, because the same determination procedure was consistently followed for all shots in a given run, the pinhole analysis will accurately identify the trends in the data.

When received for analysis, the pinhole images were on film. They were then digitized, using a Hewlett-Packard ScanJet II scanner and accompanying software. Software settings were 150 dpi, 256 black and white shades, brightness 120 and contrast 131. The choice of resolution and color bit length was made to optimize information content while keeping the file size reasonable. A full-page scan of all 12 images for a given shot typically generated a TIFF file of about 500K bytes. One pinhole image extracted from this file takes up about 41K bytes.

One possible algorithm for finding the implosion width would be to average the pixel values in the z direction, taking the width of the radiating region to be the width at the half-maximum or similar pixel value. The most important quantity for width determination is the variation in intensity from the peak, not the absolute intensity, which is more a function of the overall power of the implosion. An illustration of the method of averaging over z is shown in Fig. (6), where pinhole photographs are shown with the r -dependent averaged pixel values. For both cases shown, the z -averaged film darkens progressively until a point of maximum darkness is reached. This maximum point is taken to be the pinch center. The pinch width can be obtained by defining some fraction of the peak value as a criterion (e.g., half-maximum). This simple procedure works best with well-defined, straight implosions like that in shot 1484. Lower-contrast, kinked implosions like that of shot 1498 are more difficult to analyze.

The problem with the z -averaging method just described is that when the implosions are not straight, or when the contrast is so low that there are multiple peaks in the averaged profile, the averaging method gives unrealistically large pinch widths. To follow a crooked or kinked implosion, it is better to conduct the z average over multiple small segments, rather than over the whole pinch. After some trial, it was found that a 6-pixel long segment was optimum: for shorter segment lengths, the radial profile became erratic, while for larger segment lengths, the computed widths became larger, but at a very slow rate.

The results of this analysis for the two sets of implosions are shown in Fig. (7) and Fig. (8). In these figures are shown, as a function of z , the computed width, the contrast in the image (possible pixel values run from 0 to 255), and the position of the center point (the darkest point in the image). To obtain the pinch width, the average was taken of the widths at each point in z . These widths were determined just as was shown in Fig. (6), except that instead of averaging over the whole pinch

length, a 6-pixel average was taken. The total width included only those points with sufficiently high image contrast that the computed width was reliable (contrast > 50); in low-contrast areas, the width and center position are primarily a result of random noise.

The procedure used to determine the width of the radiating region, then, was to scan the pinhole images, extract the high-gain time-integrated pinhole image, average the pixel values over all 6-pixel long axial segments in the image, and define the width as the average of the full-width quarter-maximum (FWQM) values at each point in z where there was sufficient contrast to discern an image. The method gave consistent and reasonable values for the width for almost all of the pinhole images, even when the image contrast was too low for reliable evaluation by eye. Shots where there was a problem determining width were 1493, which was very low contrast; 1496, where evident light contamination ruined the shot image; and 1487, for which no pinhole images were available. In addition, no pinhole image was available for shot 1483, but the pinhole image from another shot with similar parameters and yield, shot 1606, was substituted.

The size for each shot of the radiating region, derived from the pinhole photograph measurements, is plotted in Fig. (9), as a function of both mass and array diameter. Generally, the radiating region contracts as the mass increases and the initial array diameter decreases. The exceptions to this rule are the two low-mass, large-diameter shots (1492 and 1493), where in any event the pinhole images were so faint as to make the diameter measurements suspect.

In principle, the length of the radiating region could be determined with the same procedure as was used for the width. In the pinhole photographs used, however, obstructions in the field of view made this impossible, and it was assumed that in every case there was K-shell radiation over the full 2 cm length of the pinch. The photographs show that this is a reasonable assumption at least in the field of view, for hot-spot formation, while occasionally evident, did not significantly reduce the axial extent of the averaged radiating region.

Results

Data interpretation followed the procedure of Coulter, Whitney and Thornhill.⁴ Basically, this procedure is to use the measurements just described and compare them with theoretical predictions for a range of densities and temperatures. Contours can be drawn in density and temperature for the observed power per unit length as well as for the observed line ratios. The place where these contours intersect marks the inferred average plasma density and temperature.

The theoretical calculations were performed for a uniformly dense, isothermal plasma of the measured diameter and 2 cm in length, which was in collisional-radiative equilibrium (CRE).⁶ Variation in opacity with size of the emission region was included in the calculation. Theoretical contours of keV power emitted per unit length are shown in Fig. (10), for a plasma diameter of

3 mm. The experimental power per unit length was obtained using the yield from Table I and the measured pulsewidth; this selects one of the contours in Fig. (10). The ratio of Ly α to He α (plus intercombination line) power was calculated in CRE,⁷ and contours are shown in Fig. (11). The experimental line ratio, obtained from Table III, selects the appropriate contour in Fig. (11). The intersection of the two selected contours marks the average plasma and density.

For example, in shot 1483 the total extent of the radiating region is 3.1 mm, the average keV power is 4.2 TW (2.1 TW/cm) and the line ratio is 1.48. The intersection of the marked contours is at an electron temperature of 600 eV and an ion density of $7 \times 10^{19} \text{ cm}^{-3}$.

Once the average density has been determined, the fraction of the mass involved in keV radiation can be estimated by comparing the mass in the radiating region (whose extent has been measured) with the total mass in the wire array. The fraction obtained in this manner might be inaccurate because of deviations from cylindrical symmetry (tending to make the calculation an overestimate) or because of radial density variations (tending to make it an underestimate). But this fraction does give some idea of the effectiveness of the machine, for the given parameters, in including all available mass in the radiation pulse.

The measurements from the data, and the plasma parameters they imply, are summarized in Table IV. The widths for both the total radiation pulse τ_{total} and for the keV radiation pulse τ_{keV} are given, with the corresponding average power given by the energy yield (from Table I) divided by the pulsewidth. The line ratio is taken from Table III, with (as in that table) the He α fraction including the intercombination line. The average diameter of the radiating region is taken to be the FWQM of the 6-pixel z-averaged digitized pinhole image, as described above. The effective energy parameter, η_{eff} , for the implosion is an estimate, based on the linear current model described above and observed stagnation position $x_f = (\text{FWQM radius})/r_0$. Those parameters are used in Eq. (11) to get the ion kinetic energy and η value. The average ion density, electron temperature, and fraction of the mass radiating in the K shell are obtained from the data measurements as just described.

From Table IV, it is evident that both the total and keV radiated power show a regular variation with mass and array diameter. The keV power is plotted against these parameters in Fig. (12). The variations in power are not explained by variations in the average density and temperature, which are shown in Fig. (13) and Fig. (14). A similar pattern is found, however, in the radiating mass fraction, shown in Fig. (15). The participating mass fraction was evidently a very important factor in determining the keV output power in these runs. The keV power is plotted as a function of mass fraction in Fig. (16); although the relationship is not monotonic, a greater mass fraction generally results in greater power output. The effect on the keV power of varying η is also shown in Fig. (16). As was expected, the greatest keV output came from the moderate- η shots, with maximum output for $6 < \eta < 8$. The same trend is seen with the calculated value η_{eff} , except that the keV power

Table IV. Results of data analysis

Shot No.	τ_{total} (ns)	Total power (TW)	τ_{keV} (ns)	keV power (TW)	Ly_{α}/He_{α} ratio	FWQM dia (cm)	η_{eff}	n_i (10^{19} cm^{-3})	T_e (eV)	K-shell fraction
1483	20	11.20	18	4.22	1.48	0.31	7.3	7.0	600	0.72
1484	25	9.68	22	1.73	1.26	0.21	7.4	7.0	540	0.23
1487	25	11.64	20	1.50	1.39	0.20 ^(a)	3.9 ^(a)	6.1	600	0.12
1488	30	7.47	23	0.87	1.32	0.19	3.2	4.5	620	0.06
1489	51	5.29	31	0.43	1.26	0.19	2.8	2.0	830	0.02
1498	87	2.62	32	0.15	1.25	0.09	2.7	2.7	760	0.004
1492	29	5.93	25	0.32	1.24	0.12	43.2	3.5	700	0.15
1493	26	6.54	27	0.45	1.27	0.24	25.4	1.7	900	0.21
1494	27	7.26	26	0.86	1.58	0.45	15.7	1.2	1150	0.46
1495	22	15.05	19	3.33	1.37	0.41	9.1	4.3	620	0.78
1496	36	10.11	32	1.91	1.06	0.32 ^(b)	7.1	5.0	500	0.38
1497	38	8.89	36	0.84	1.00	0.28	4.9	2.8	600	0.10

^(a) No pinhole data; value inferred from trend

^(b) Unreliable data: Actual image is washed out

maximum occurs at $\eta_{eff} \approx 10$.

Conclusions

In these experiments, the total implosion kinetic energy was held constant, while mass and initial radius were varied over a wide range. A detailed and consistent analysis of the experimental data was conducted to estimate the average plasma parameters during the implosion, and to investigate trends in these that could explain the variation in keV radiated power.

As is shown in Fig. (16), both the average energy per particle, represented by η , and the fraction of the array mass participating in the implosion showed a clear relationship to the keV radiated power. No such simple relationship was found with other plasma parameters. The consideration of mass participation could be particularly important on high-power, short-pulsewidth machines like Saturn.² With a short pulsewidth, mass participation could be reduced by incomplete wire vaporization, and initial nonuniformities in plasma temperature and density will be more pronounced, affecting current penetration and implosion dynamics. At high power levels, both macro- and micro-instabilities may complicate the implosion dynamics, and L- and M-shell losses could become significant during the implosion.

The results presented here can only provide information on the “average” state of the plasma during the implosion. Lacking data with significant time and spatial resolution, we could not consider the significant time variations in plasma conditions and radiation; nor could we include the significant gradients in temperature, density, and electric and magnetic fields that occur during the

implosion. Still, these self-consistent calculations provide valuable insight into the average plasma conditions during the radiation pulse, and also provide a consistent means of comparing different PRS implosions. To understand the impact of dynamic variations and spatial gradients, MHD simulations³ can be used to generate data for known implosion parameters that can be analyzed with the same procedures given here (such an effort is currently underway). As temporally- and spatially-resolved experimental measurements become available, the procedures detailed here can be readily used to provide rapid analysis of the data.

References

1. K.G. Whitney, J.W. Thornhill, R.B. Spielman, T.J. Nash, J.S. McGurn, L.E. Ruggles and M.C. Coulter, "Analysis of recent Saturn aluminum PRS experiments," in *Dense Z-pinches*, Third International Conference, London, 1993, ed. by M. Haines and A. Knight, AIP Conf. Proc. No. 299 (AIP, New York), pg. 429 (1994).
2. K.G. Whitney, J.W. Thornhill, J.L. Giuliani, Jr., J. Davis, L.A. Miles, E.E. Nolting, V.L. Kenyon, W.A. Spicer, J.A. Draper, C.R. Parsons, P. Dang, R.B. Spielman, T.J. Nash, J.S. McGurn, L.E. Ruggles, C. Deeney, R.R. Prasad and L. Warren, *Phys. Rev. E* **50**,2166 (1994).
3. K.G. Whitney, J.W. Thornhill, J.P. Apruzese and J. Davis, *J. Appl. Phys.* **67**,1725 (1990).
4. M.C. Coulter, K.G. Whitney and J.W. Thornhill, *J. Quant. Spectrosc. Radiat. Transfer* **44**,443 (1990); M.C. Coulter, K.G. Whitney and N.G. Loter, "Analysis of Maxwell Laboratory Wire Experiments", NRL Memorandum Report 6383 (1988).
5. J. Katzenstein, *J. Appl. Phys.* **52**,676 (1981).
6. K.G. Whitney and P.C. Kepple, *J. Quant. Spectrosc. Radiat. Transfer* **27**,281 (1982).
7. J.P. Apruzese, D. Duston and J. Davis, *J. Quant. Spectrosc. Radiat. Transfer* **36**,339 (1986).

Implosion position and velocity with Linear current rise

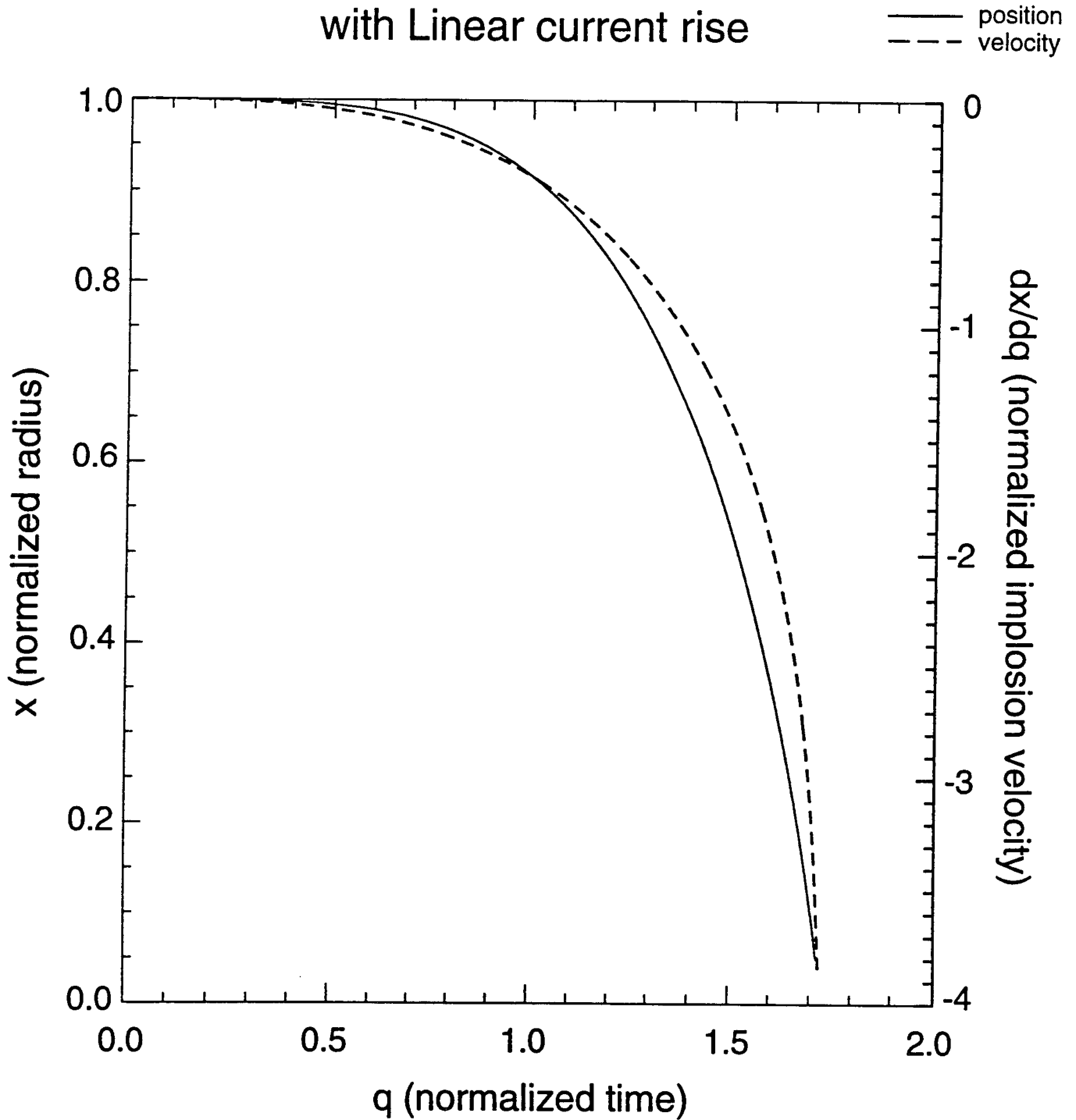


Figure 1. Solution to Eq. (9) for normalized radial position $x = r/r_0$ and normalized implosion velocity dx/dq , as a function of normalized time q , given by Eq. (10). In the linear-current model, every implosion follows these curves until $x = x_f$, where x_f is defined to be the stagnation point.

PCD OUTPUT - SET 1

— keV
- - - Total

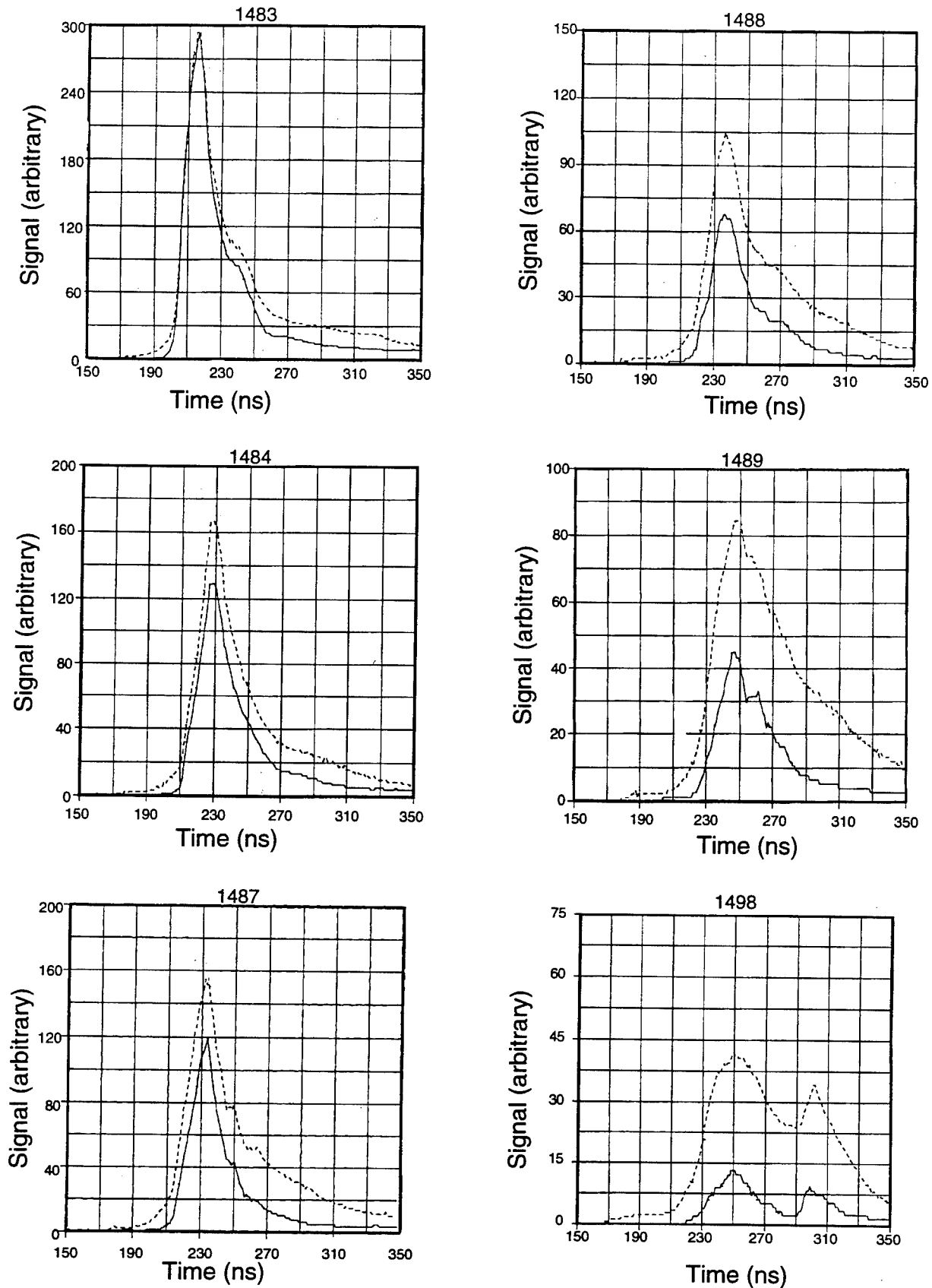


Figure 2a. X-ray photodetector output for each experimental shot, used to determine the x-ray pulsewidth. The total signal is given by the dashed lines, and the filtered keV signal is given by solid lines. The set grouping is given in Table I.

PCD OUTPUT - SET 2

— keV
- - - Total

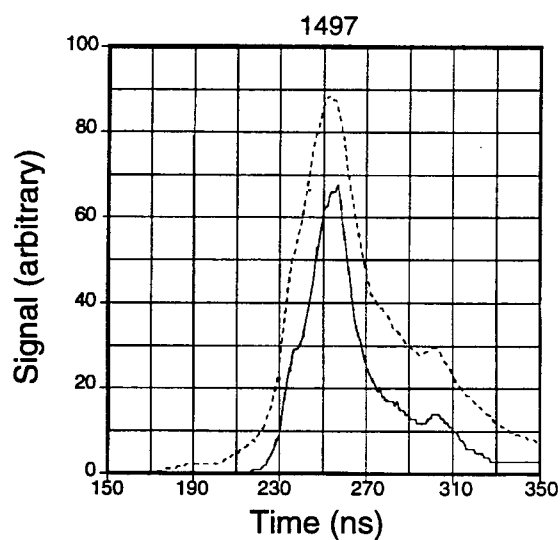
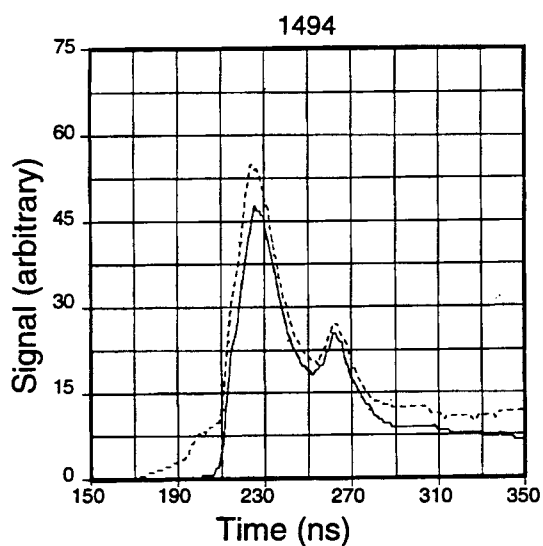
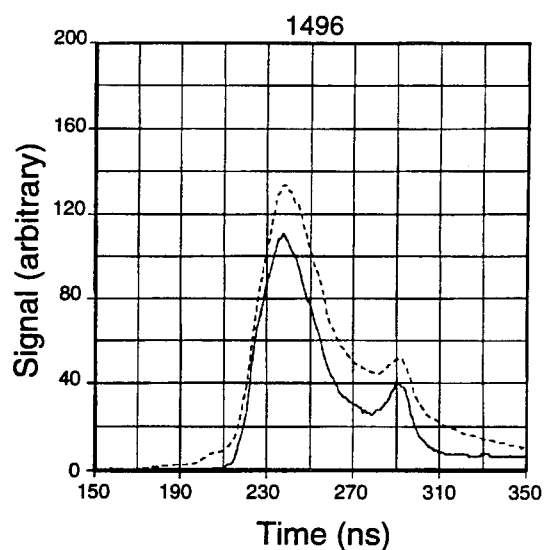
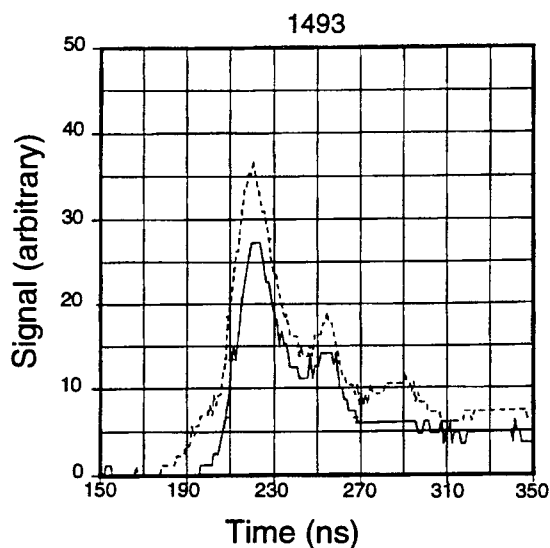
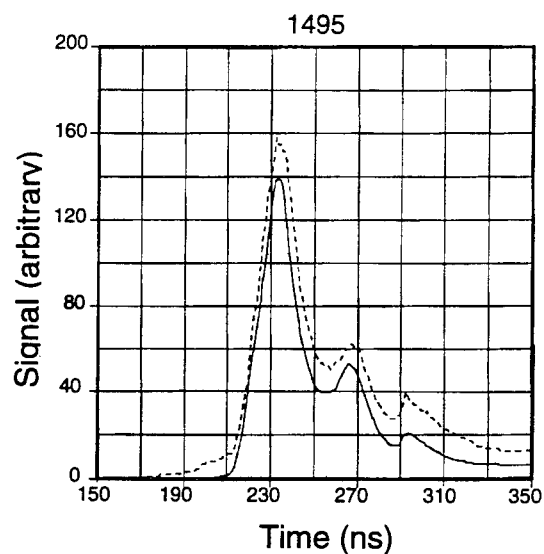
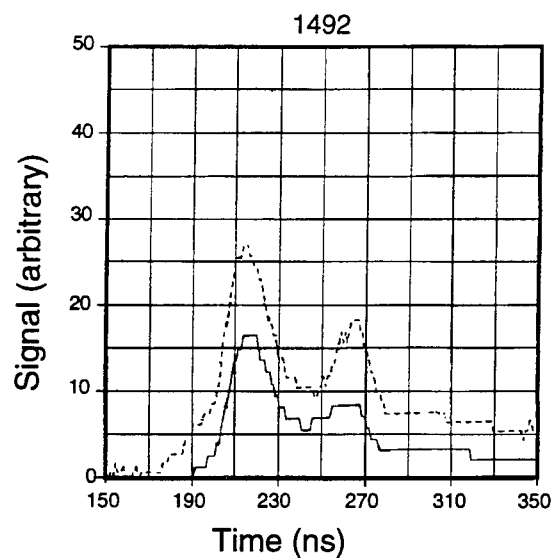


Figure 2b. X-ray photodetector output for each experimental shot, used to determine the x-ray pulsewidth. The total signal is given by the dashed lines, and the filtered keV signal is given by solid lines. The set grouping is given in Table I.

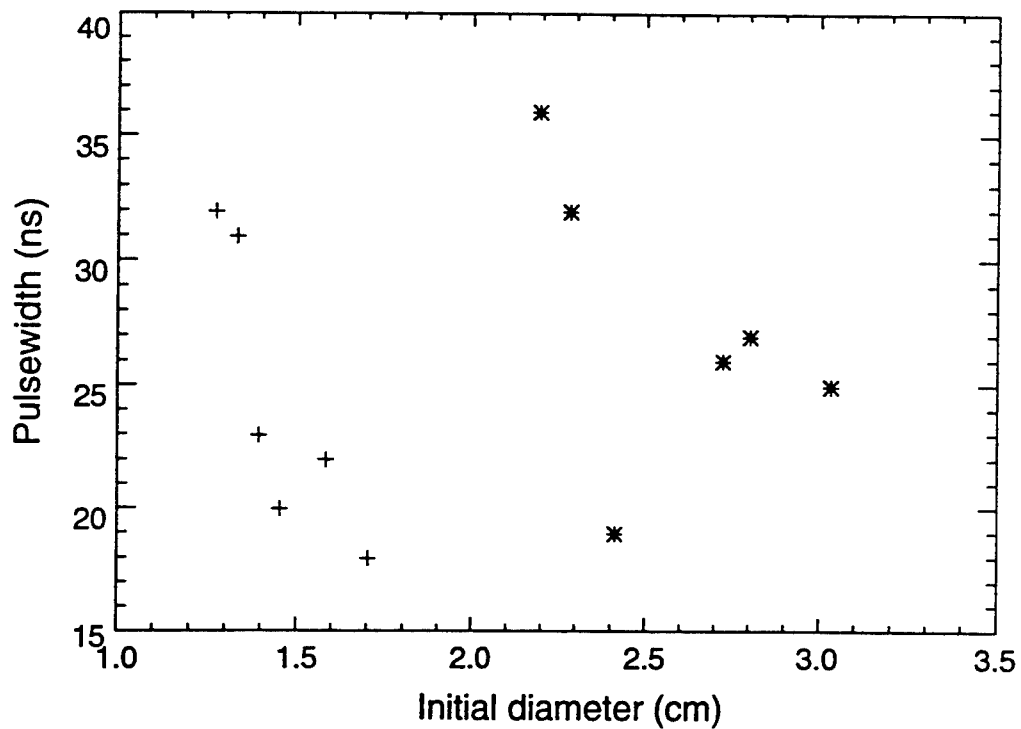
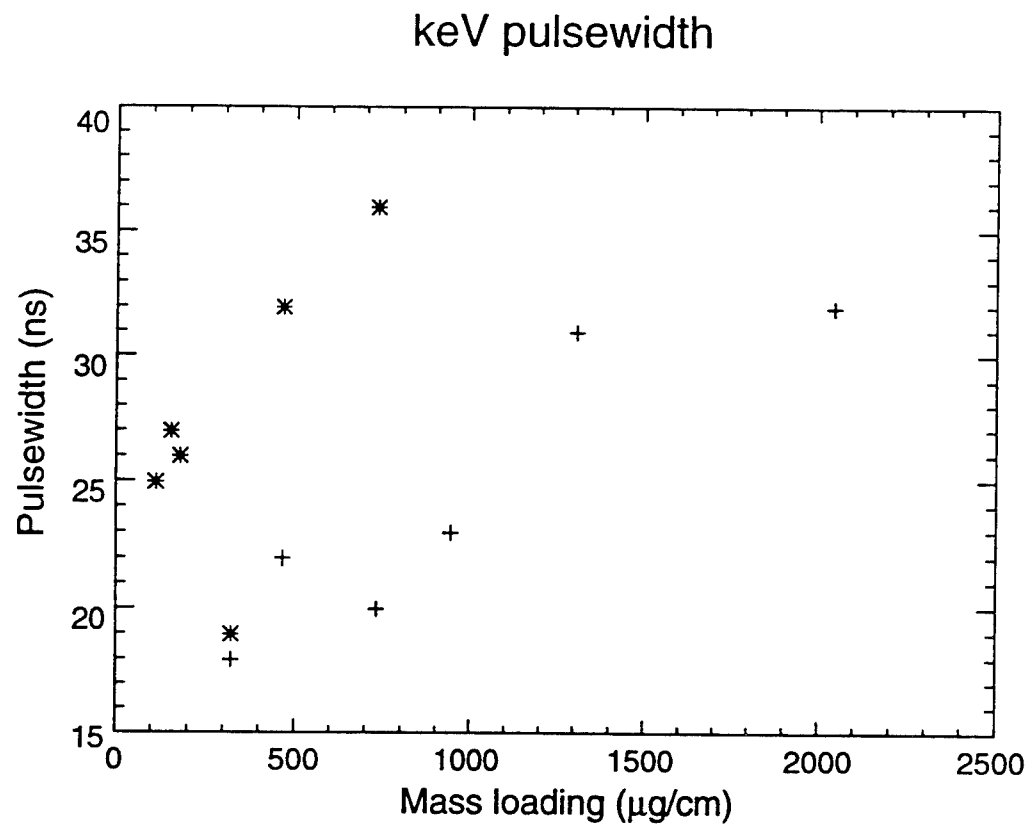


Figure 3. The keV pulsewidth, measured from Fig. (2) as described in the text, plotted as a function of array linear mass density and initial array diameter. Points from data set 1 (see Table I) are plotted with a plus sign (+), and points from data set 2 are plotted with a star (*).

SET 1 SPECTRA

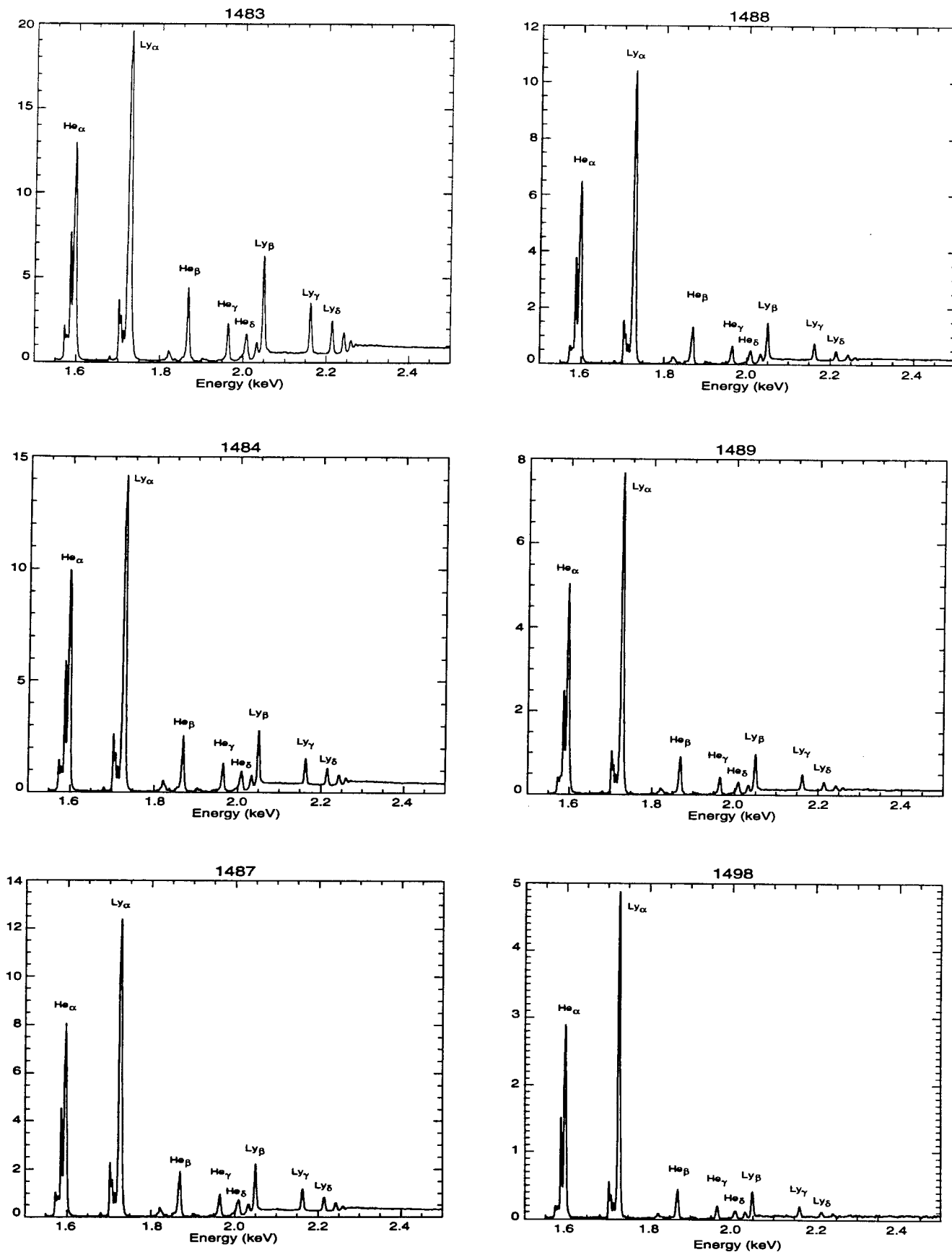


Figure 4a. Measured spectra for each experimental shot. Important lines (listed in Table II) are identified. The set grouping is given in Table I.

SET 2 SPECTRA

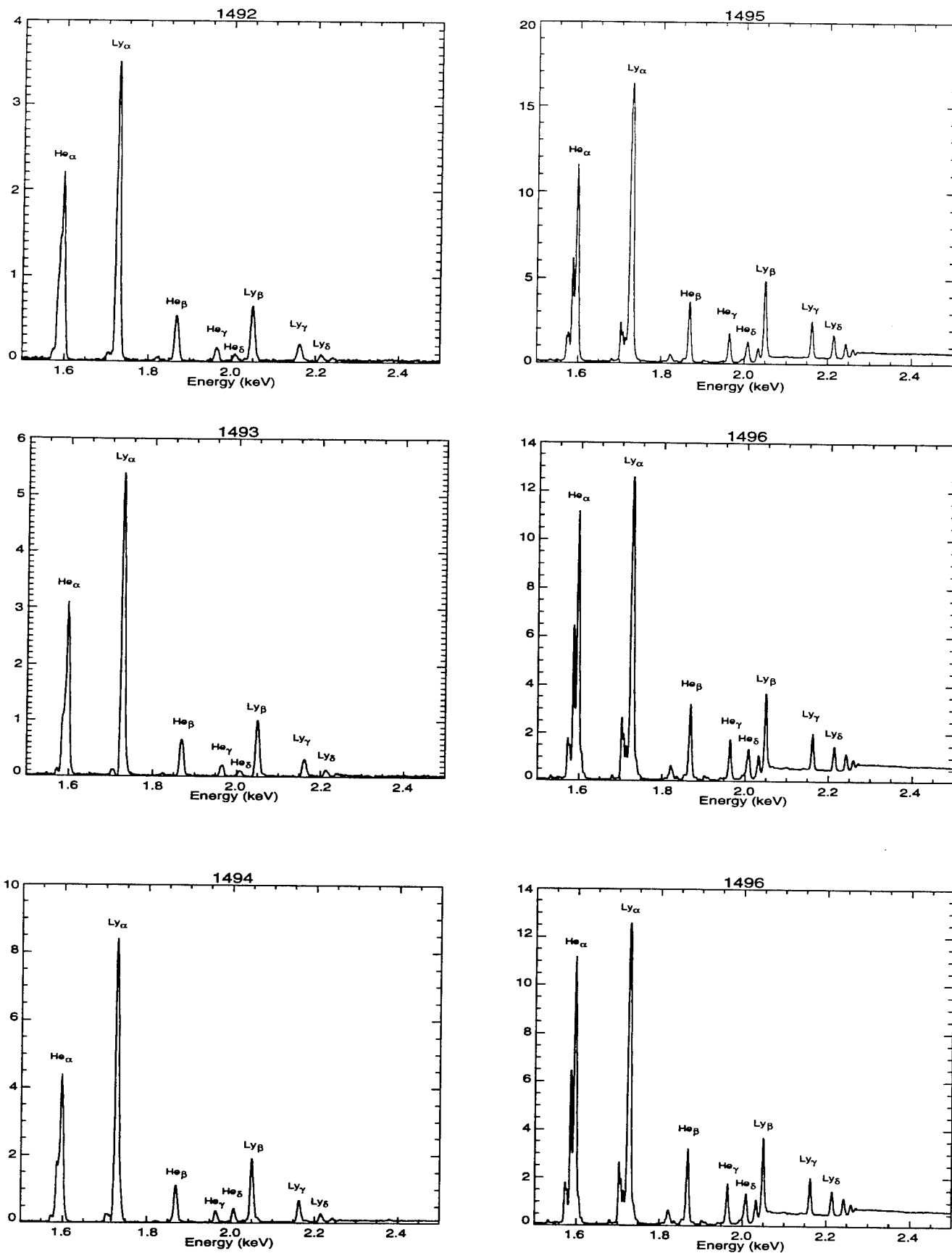


Figure 4b. Measured spectra for each experimental shot. Important lines (listed in Table II) are identified. The set grouping is given in Table I.

SET 1 INTEGRATED SPECTRA

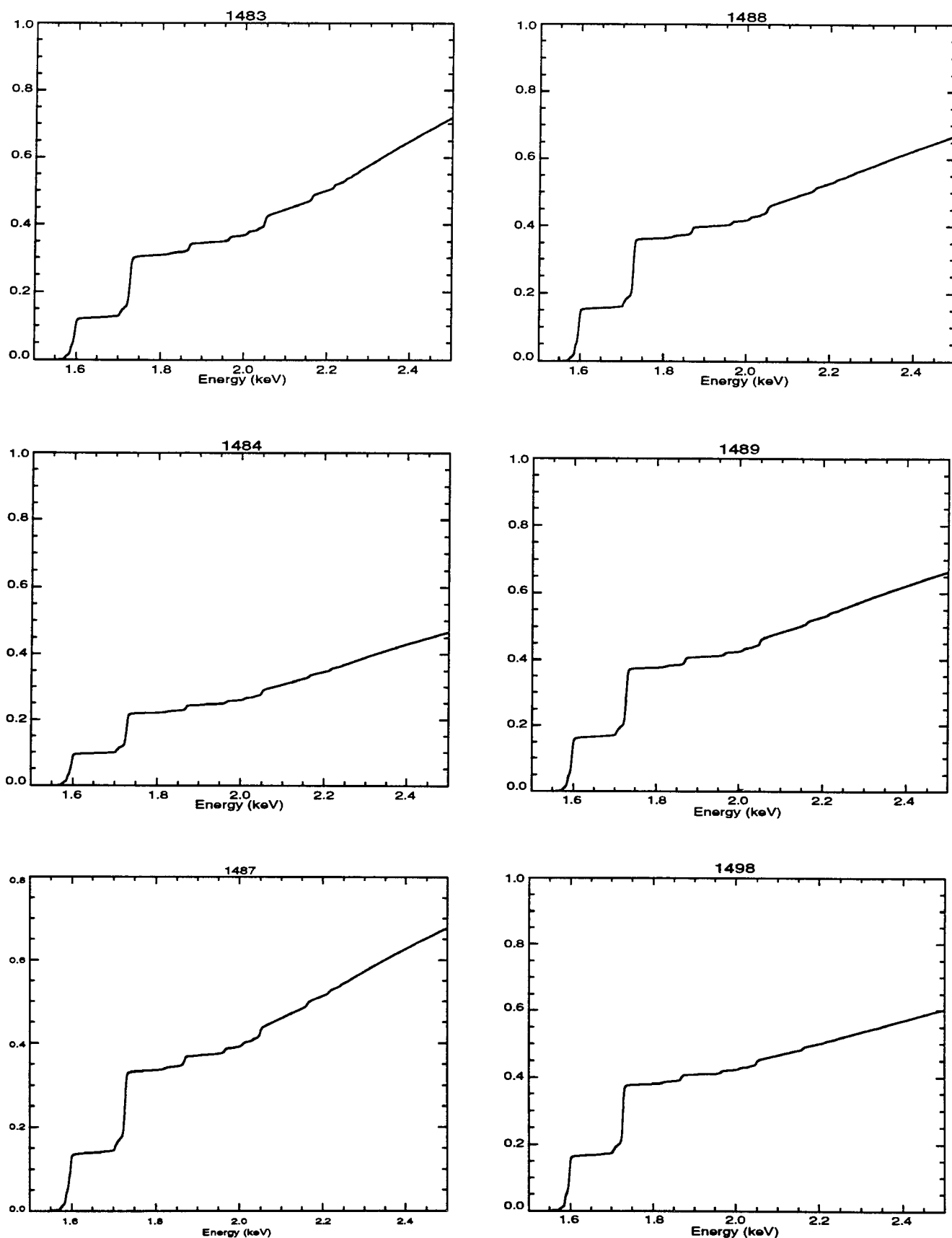


Figure 5a. Integral under the curve of each of the spectra in Fig. (4), and used in the data analysis. The power emitted in each spectral line is proportional to the rise in the integral curve over the width of that line. Prominent peaks in Fig. (4) are associated with a steep slope in the integral curves. The set grouping is given in Table I.

SET 2 INTEGRATED SPECTRA

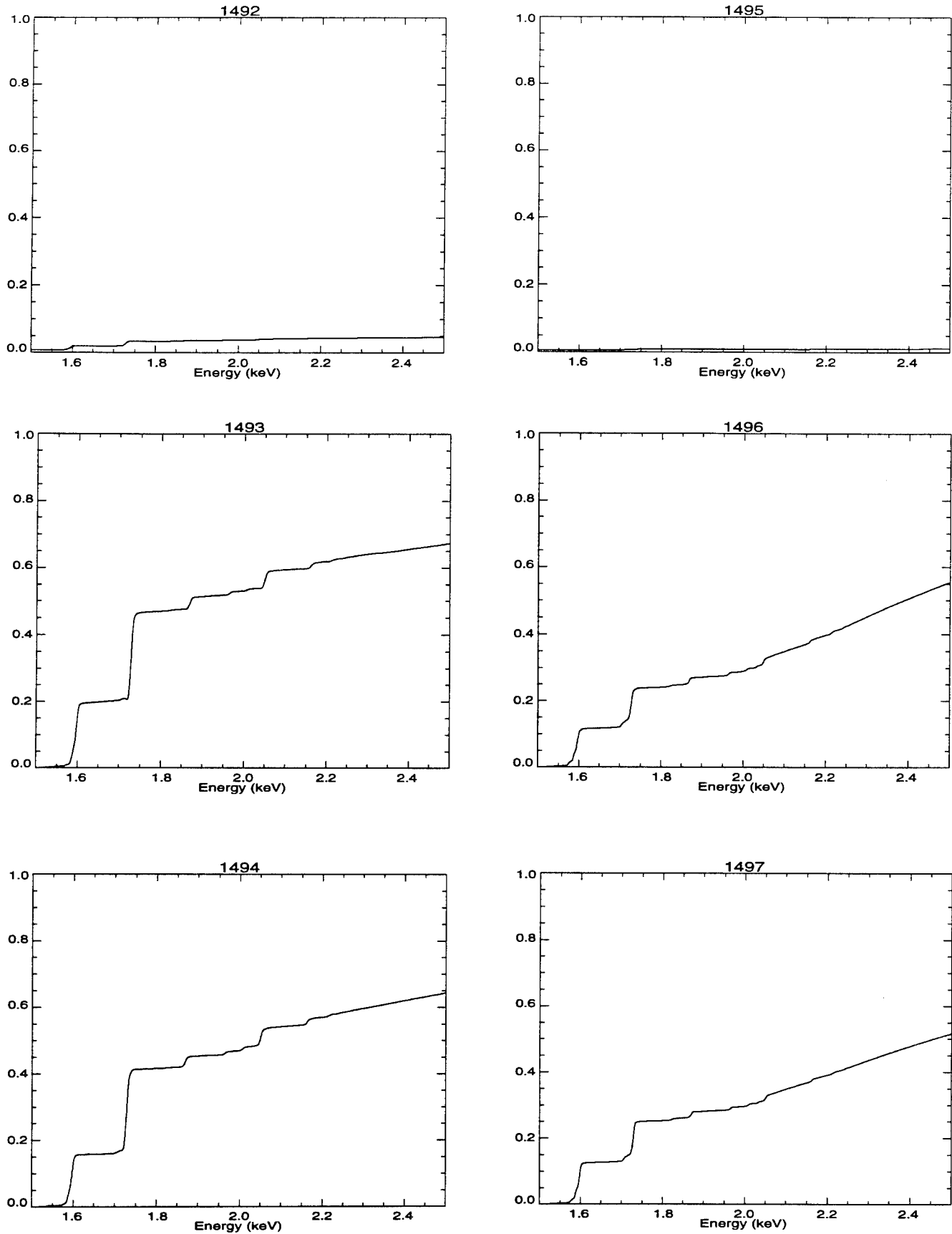


Figure 5b. Integral under the curve of each of the spectra in Fig. (4b), and used in the data analysis. The power emitted in each spectral line is proportional to the rise in the integral curve over the width of that line. Prominent peaks in Fig. (4b) are associated with a steep slope in the integral curves. The set grouping is given in Table I.

Radial profile with axial averaging

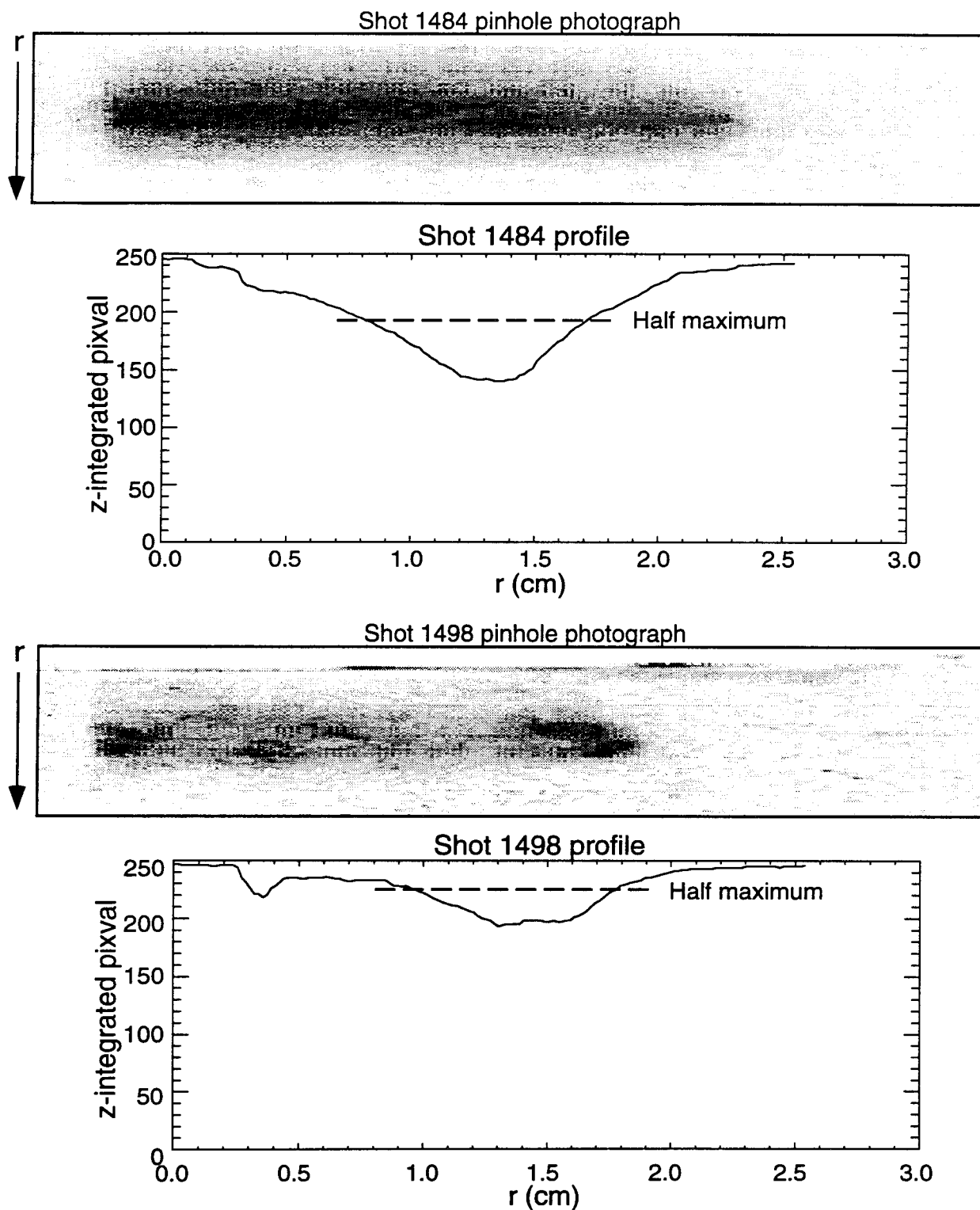
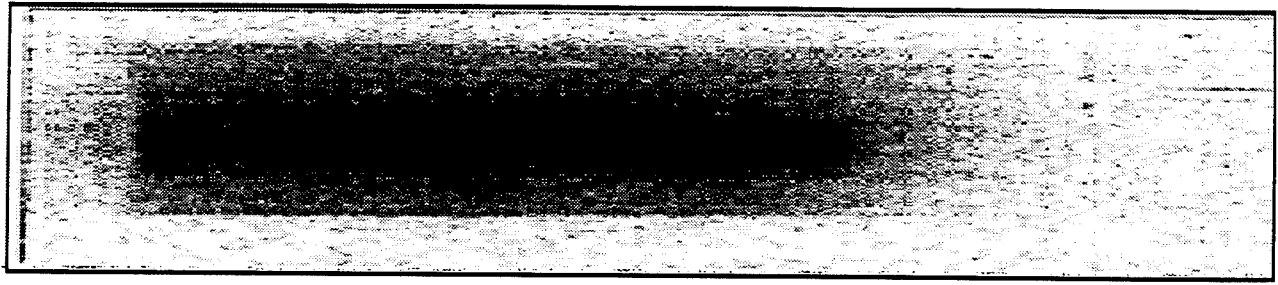


Figure 6. Two illustrations of the method of determining the width of the radiating region by averaging the film darkness in the axial (z) direction. Radial coordinates given here measure distance on the film, which is twice the actual experimental distance. At the top is the pinhole photograph and corresponding radial profile for shot 1484, a fairly well-defined, straight implosion. When averaged in z , the pixel values (black=0, white=255) form a well-defined, comparatively narrow peak, from which a "pinch radius" can be obtained. At the bottom is the same information for shot 1498, an implosion which is still fairly well-defined, but which has noticeable bends and hot-spots. For this shot, the pinch profile is broad, and has two peaks, making determination of the pinch boundaries much more difficult.

Pinhole photograph for shot 1606



i1606.TIFF150; Rows: 151, columns: 270; cm/line: 0.016933 WD 6

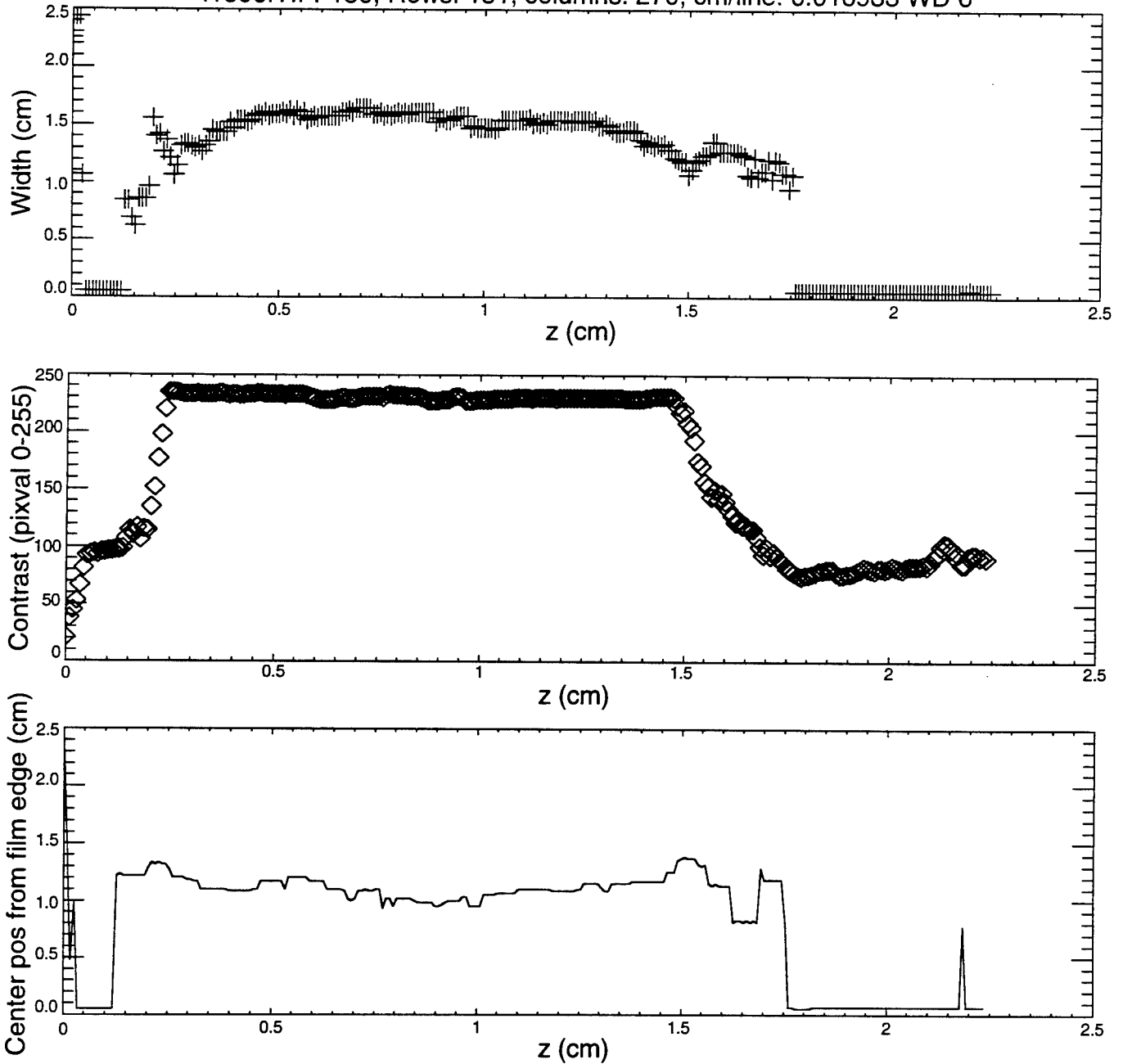
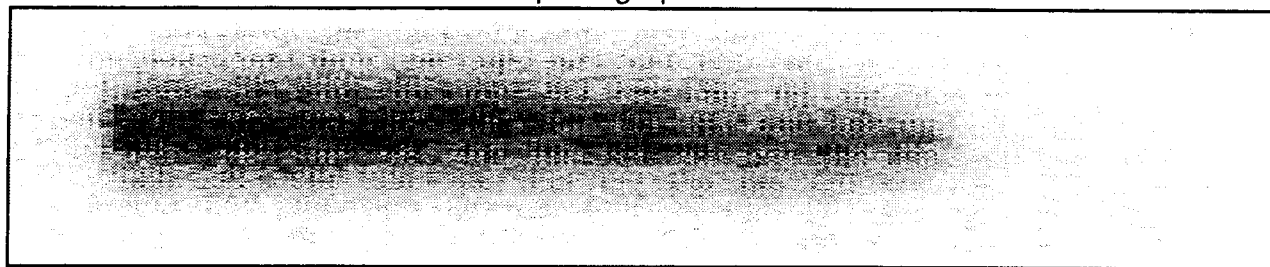


Figure 7a. Pinhole photograph and analysis from shot 1606, having similar parameters to shot 1483 (for which there was no pinhole data). Shown, as a function of axial position z are 1) pinhole photograph; 2) pinch diameter, determined as described in the text; 3) image contrast (maximum 255); 4) position of darkest point ("center" of pinch). The overall pinch width was taken to be the average of the values in (2), except that points were not included when contrast was less than 50. The center-point position gives some indication of pinch straightness.

Pinhole photograph for shot 1484



i1484.TIFF150; Rows: 151, columns: 270; cm/line: 0.016933 WD 6

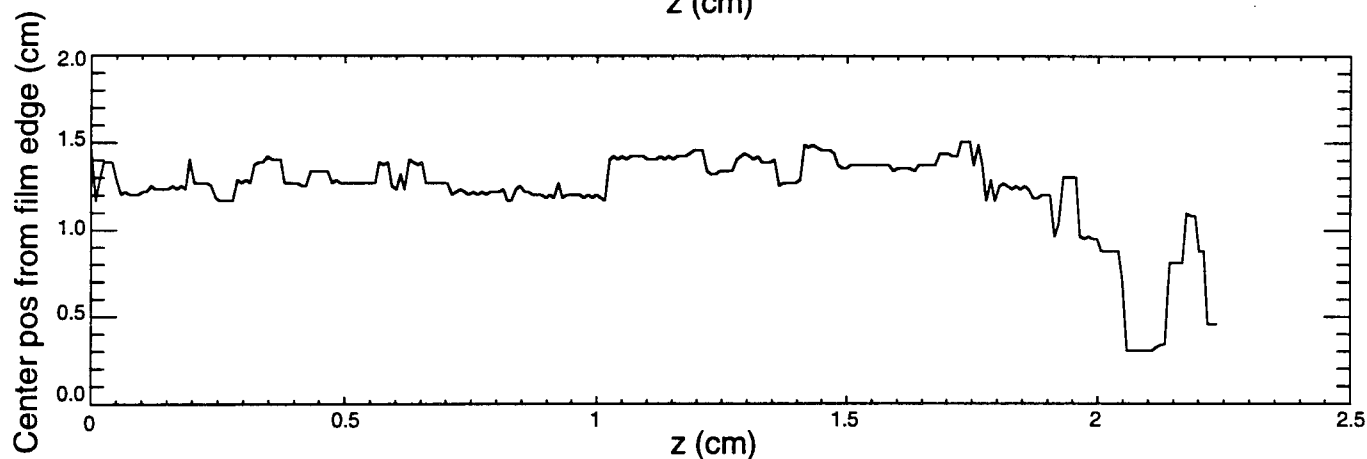
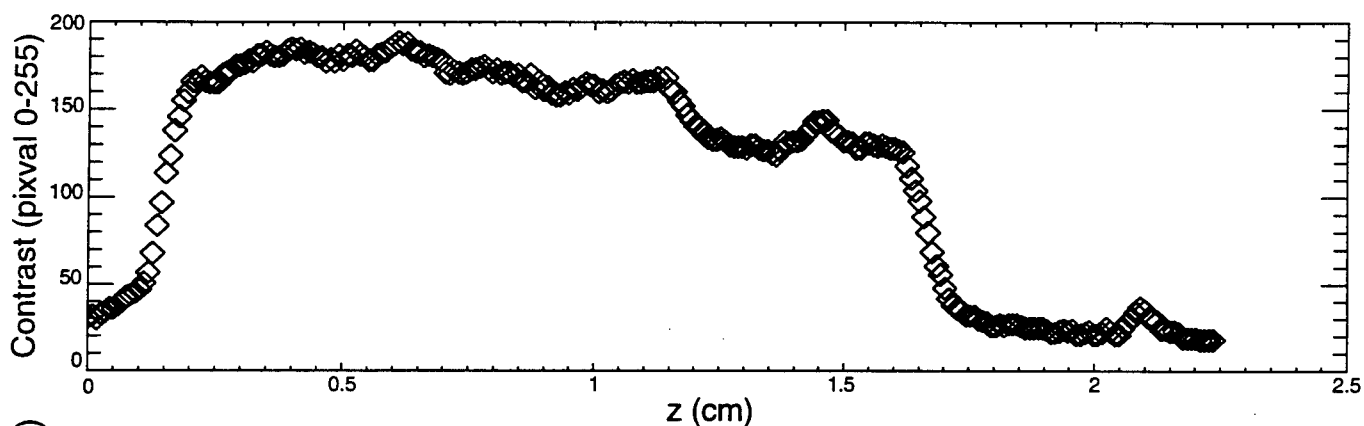
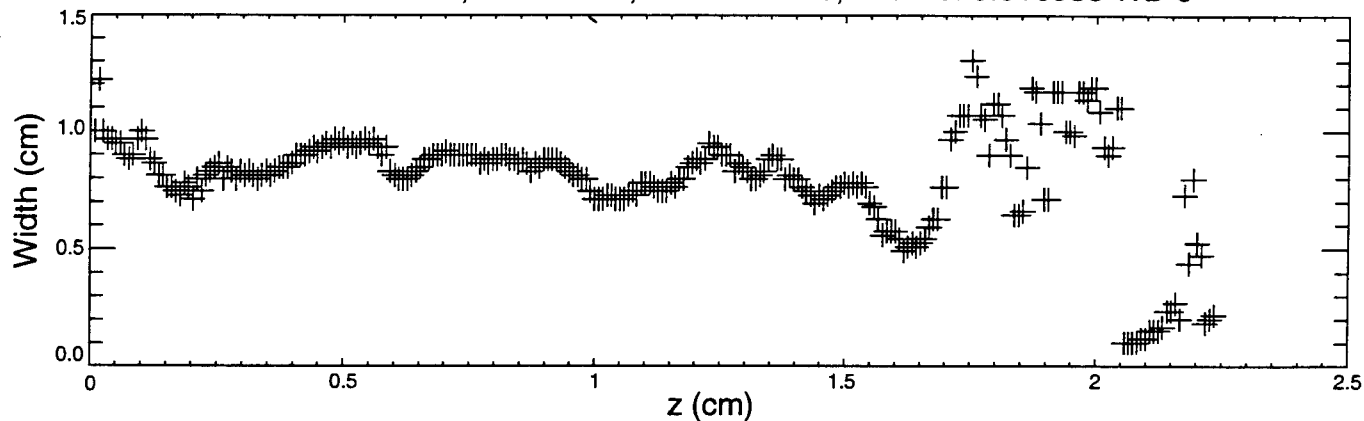


Figure 7b. Pinhole photograph and analysis from shot 1484. Shown, as a function of axial position z are 1) pinhole photograph; 2) pinch diameter, determined as described in the text; 3) image contrast (maximum 255); 4) position of darkest point ("center" of pinch). The overall pinch width was taken to be the average of the values in (2), except that points were not included when contrast was less than 50. The center-point position gives some indication of the straightness of the pinch.

Pinhole photograph for shot 1488



i1488.TIFF150; Rows: 151, columns: 270; cm/line: 0.016933 WD 6

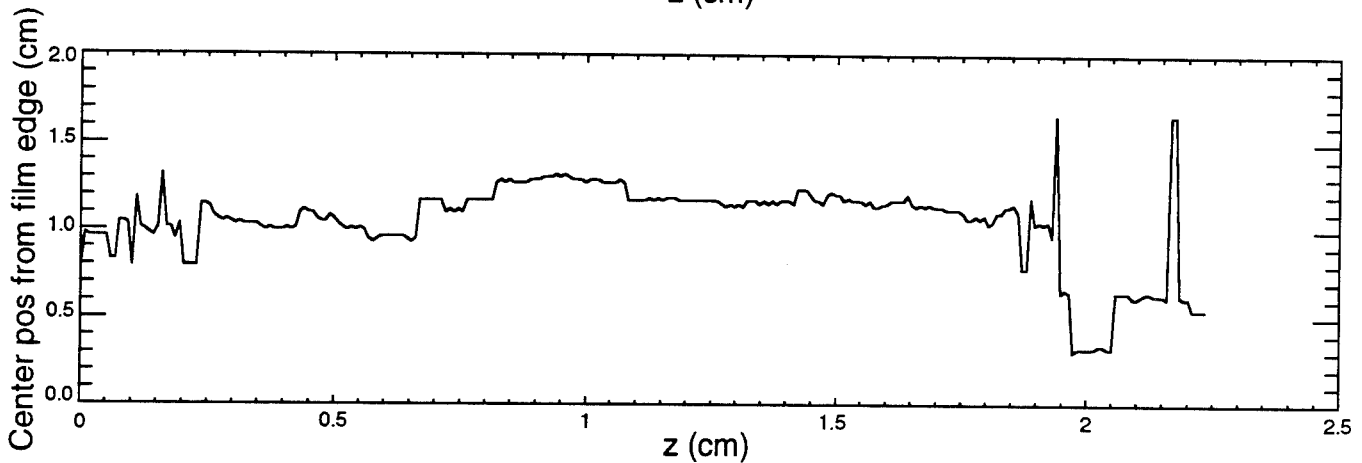
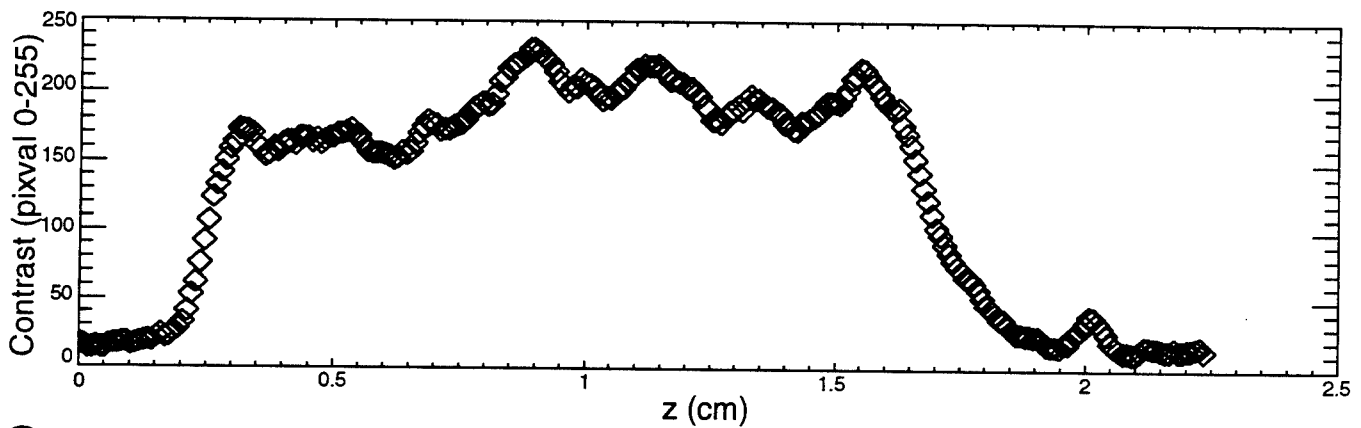
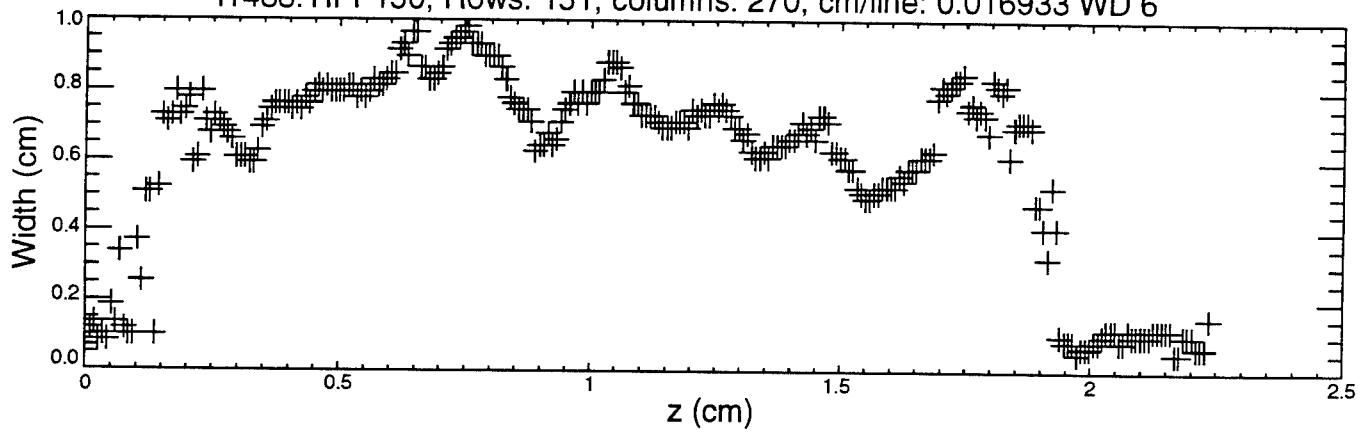


Figure 7c. Pinhole photographs and analysis from shot 1488. Shown, as a function of axial position z are 1) pinhole photograph; 2) pinch diameter, determined as described in the text; 3) image contrast (maximum 255); 4) position of darkest point ("center" of pinch). The overall pinch width was taken to be the average of the values in (2), except that points were not included when contrast was less than 50. The center-point position gives some indication of the straightness of the pinch.

Pinhole photograph for shot 1489



i1489.TIFF150; Rows: 151, columns: 270; cm/line: 0.016933 WD 6

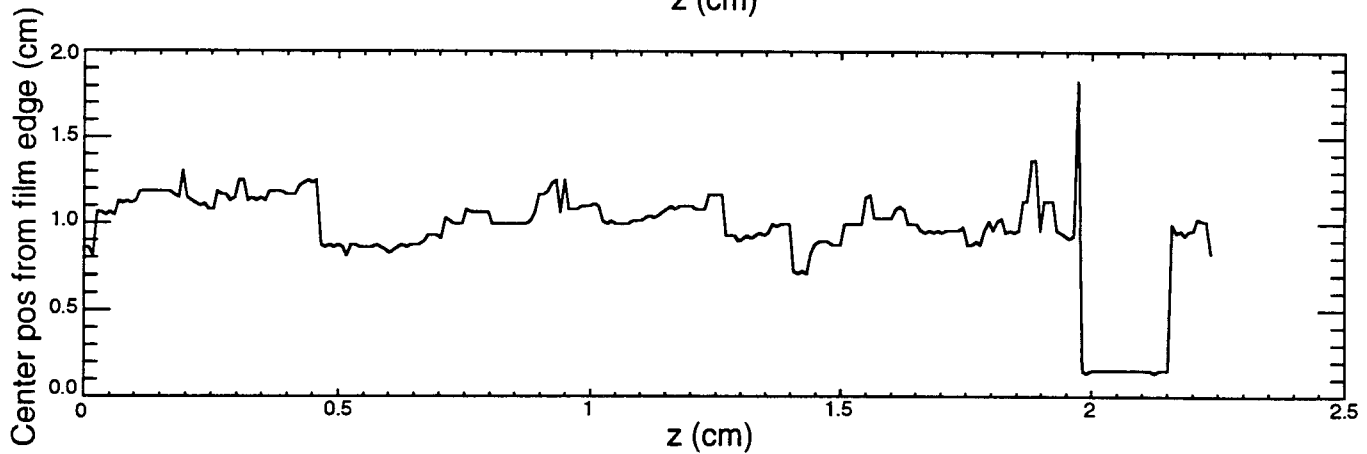
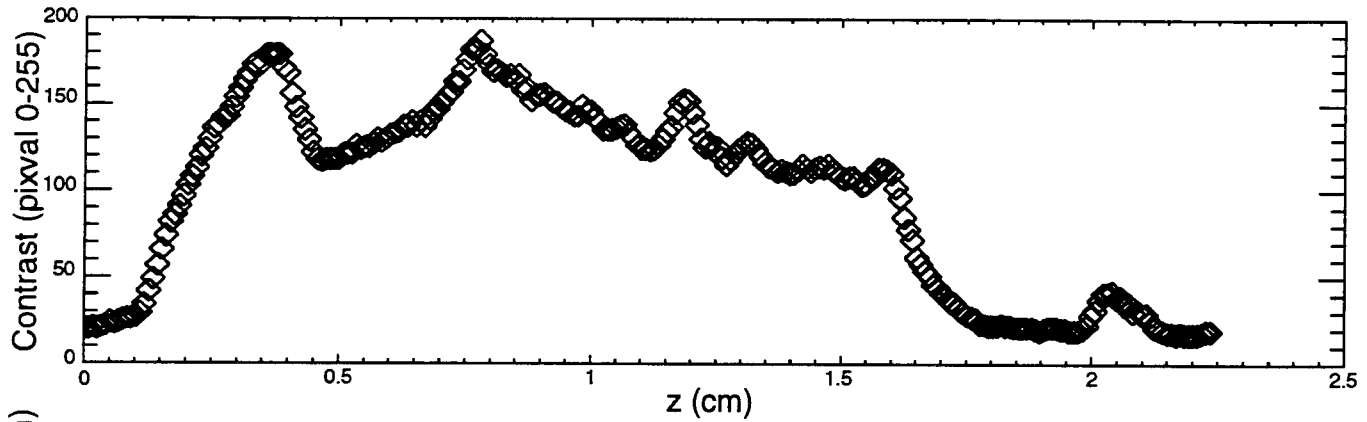
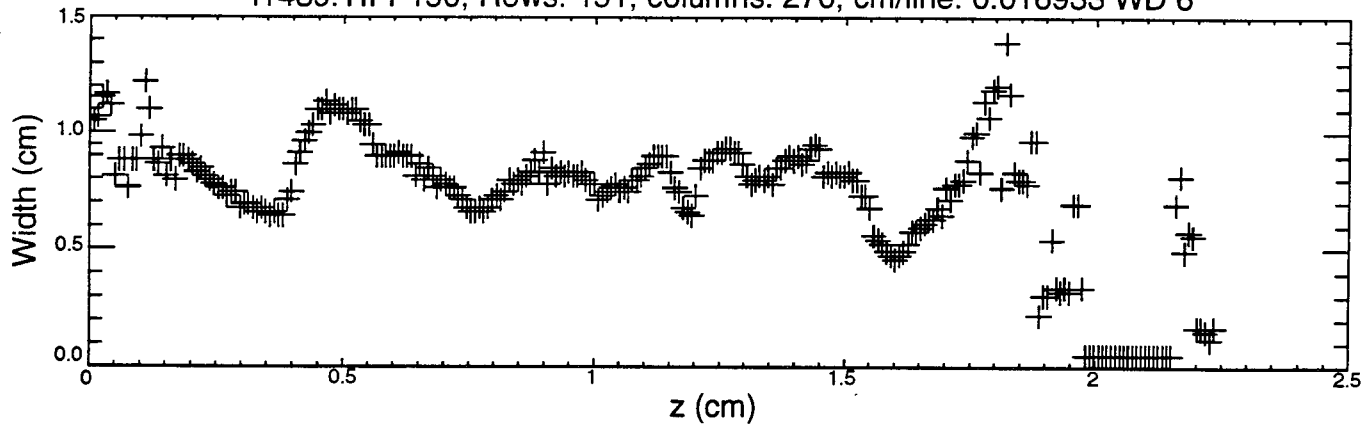


Figure 7d. Pinhole photograph and analysis from shot 1489. Shown, as a function of axial position z are
 1) pinhole photograph; 2) pinch diameter, determined as described in the text; 3) image contrast (maximum 255);
 4) position of darkest point ("center" of pinch). The overall pinch width was taken to be the average of the values
 in (2), except that points were not included when contrast was less than 50. The center-point position gives some
 indication of the straightness of the pinch.

Pinhole photograph for shot 1498

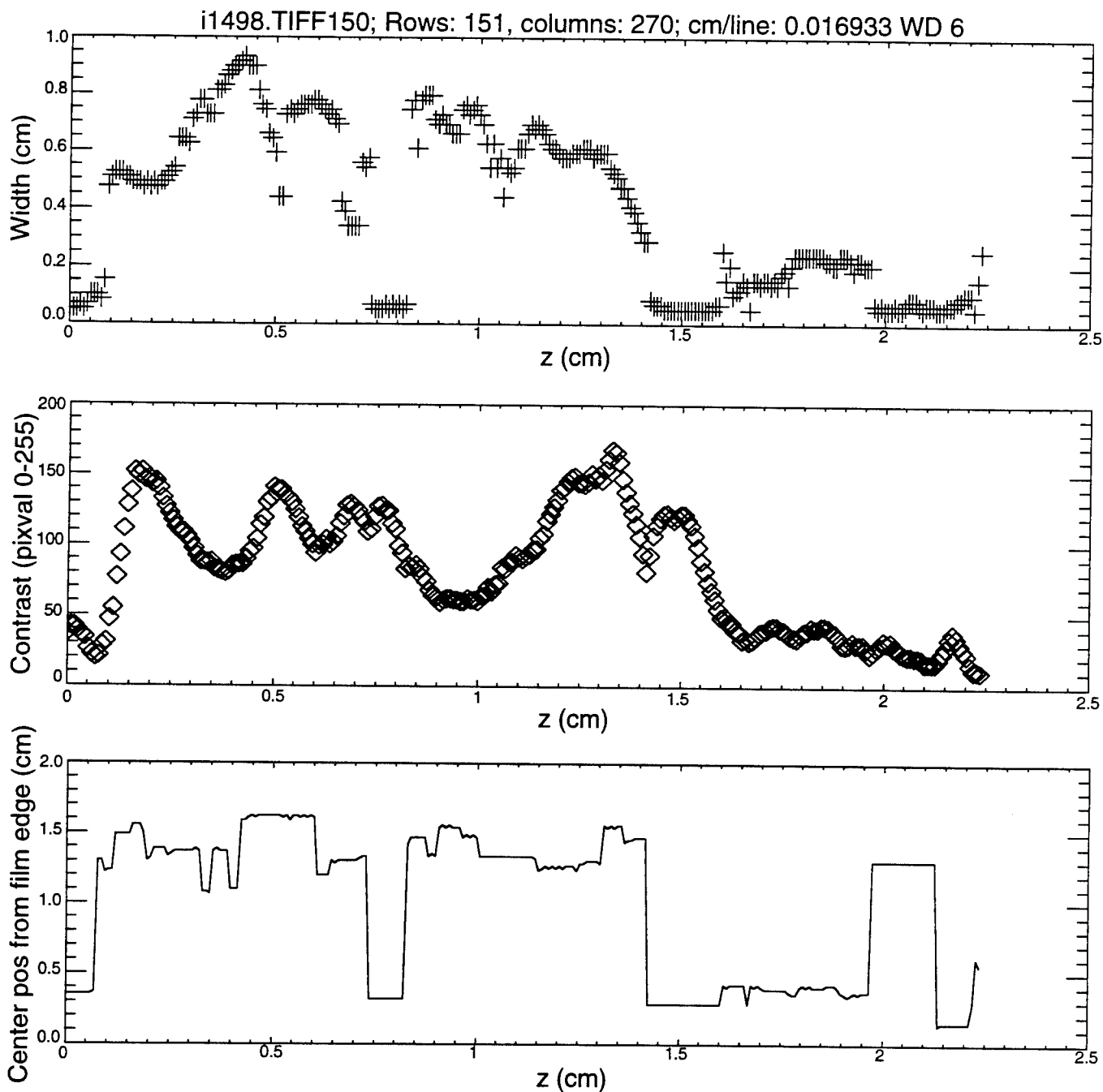
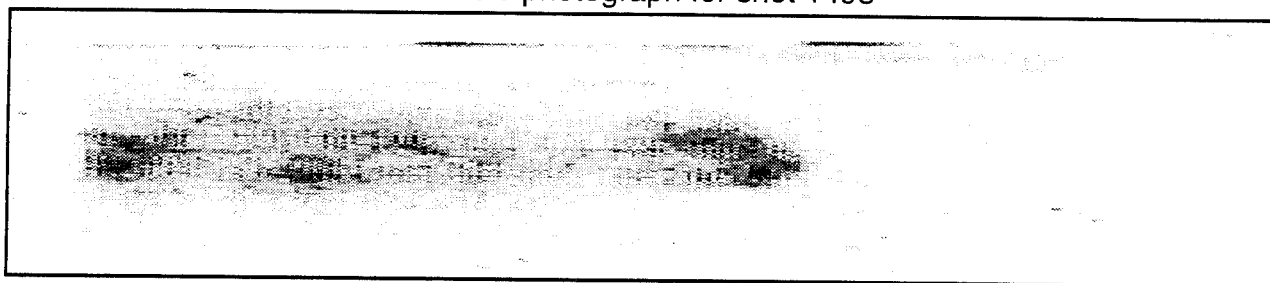


Figure 7e. Pinhole photograph and analysis from shot 1498. Shown, as a function of axial position z are 1) pinhole photograph; 2) pinch diameter, determined as described in the text; 3) image contrast (maximum 255); 4) position of darkest point ("center" of pinch). The overall pinch width was taken to be the average of the values in (2), except that points were not included when contrast was less than 50. The center-point position gives some indication of the straightness of the pinch.

Pinhole photograph for shot 1492

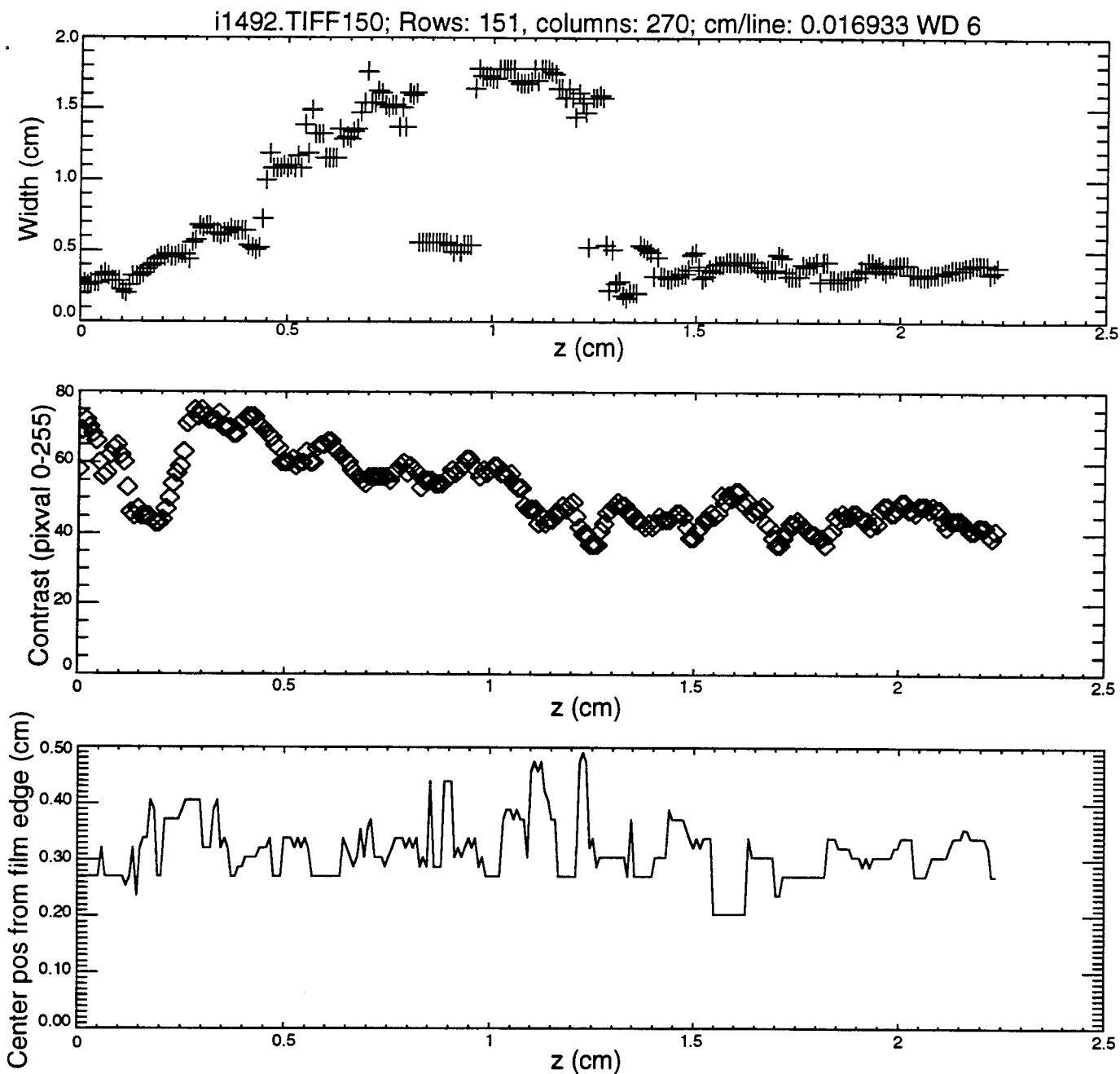
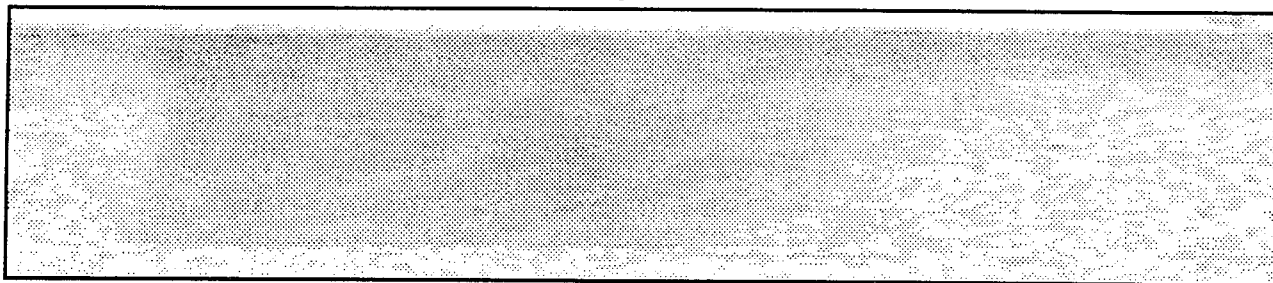


Figure 8a. Pinhole photograph and analysis from shot 1492. Shown, as a function of axial position z are
 1) pinhole photograph; 2) pinch diameter, determined as described in the text; 3) image contrast (maximum 255);
 4) position of darkest point ("center" of pinch). The overall pinch width was taken to be the average of the values
 in (2), except that points were not included when contrast was less than 50. The center-point position gives some
 indication of the straightness of the pinch.

Pinhole photograph for shot 1493

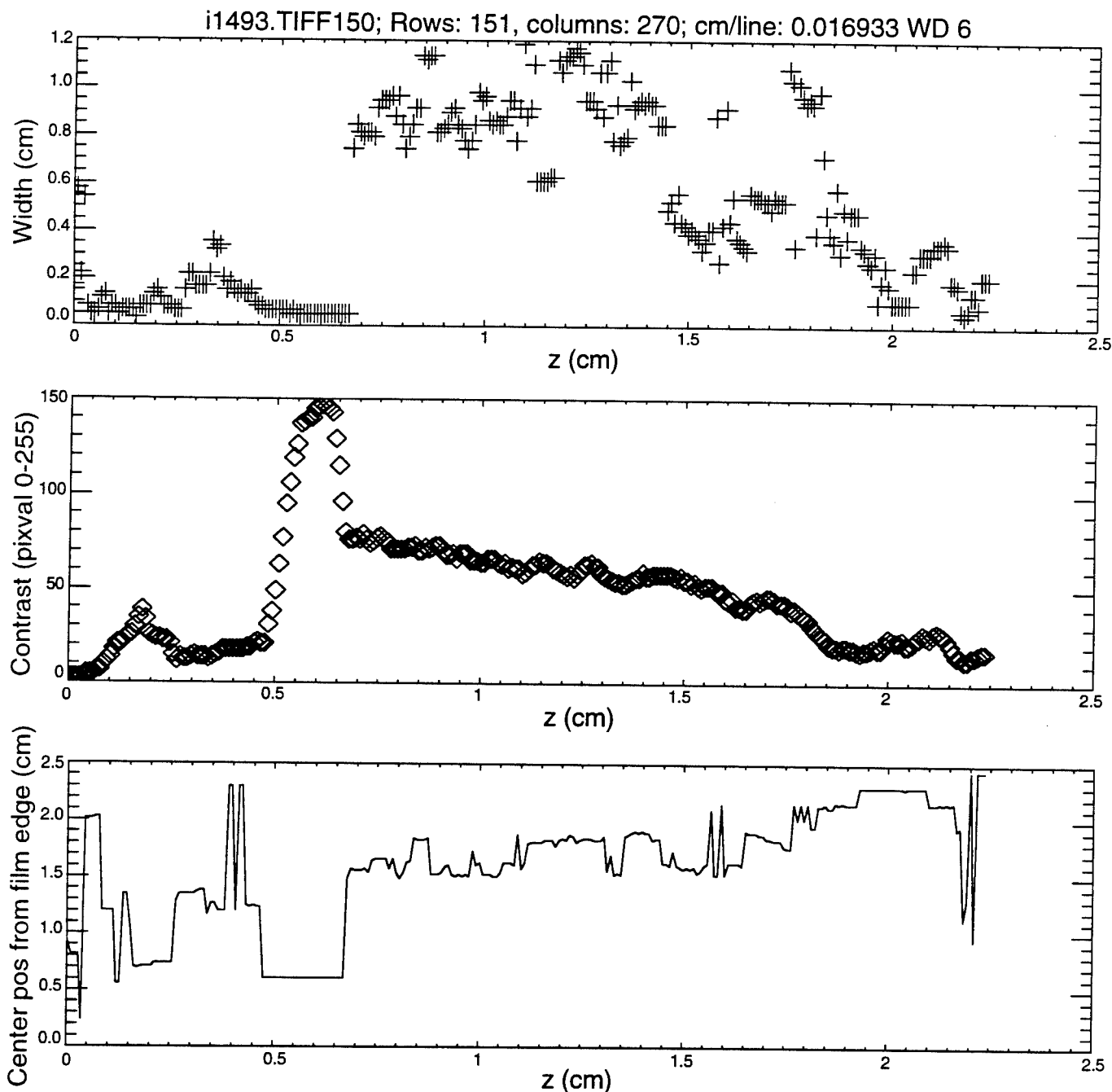
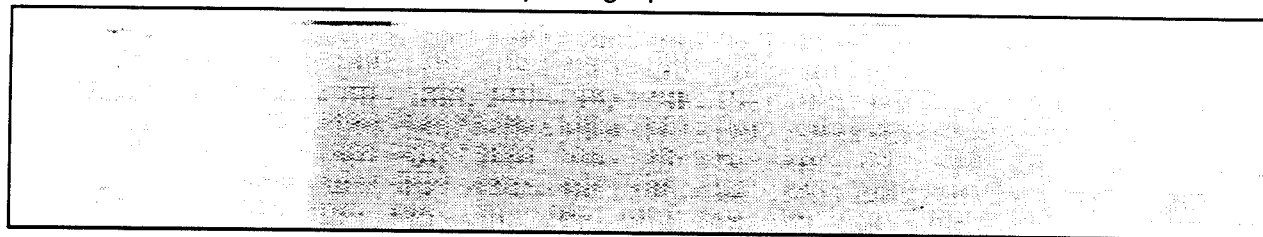
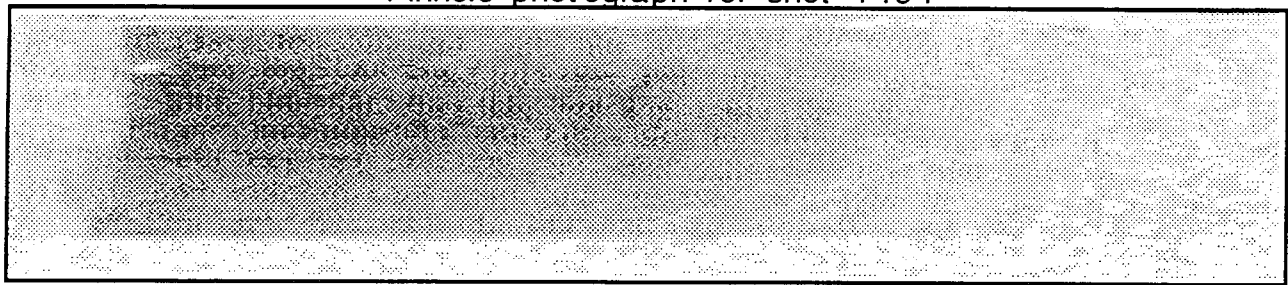


Figure 8b. Pinhole photograph and analysis from shot 1493. This low-contrast shot shows a discernible pinch radius, but suffers from noise around $z=0.6$ cm. Shown, as a function of axial position z are 1) pinhole photograph; 2) pinch diameter, determined as described in the text; 3) image contrast (maximum 255); 4) position of darkest point ("center" of pinch). The overall pinch width was taken to be the average of the values in (2), except that points were excluded when contrast was less than 50. The center-point position gives some indication of pinch straightness.

Pinhole photograph for shot 1494



i1494.TIFF150; Rows: 151, columns: 270; cm/line: 0.016933 WD 6

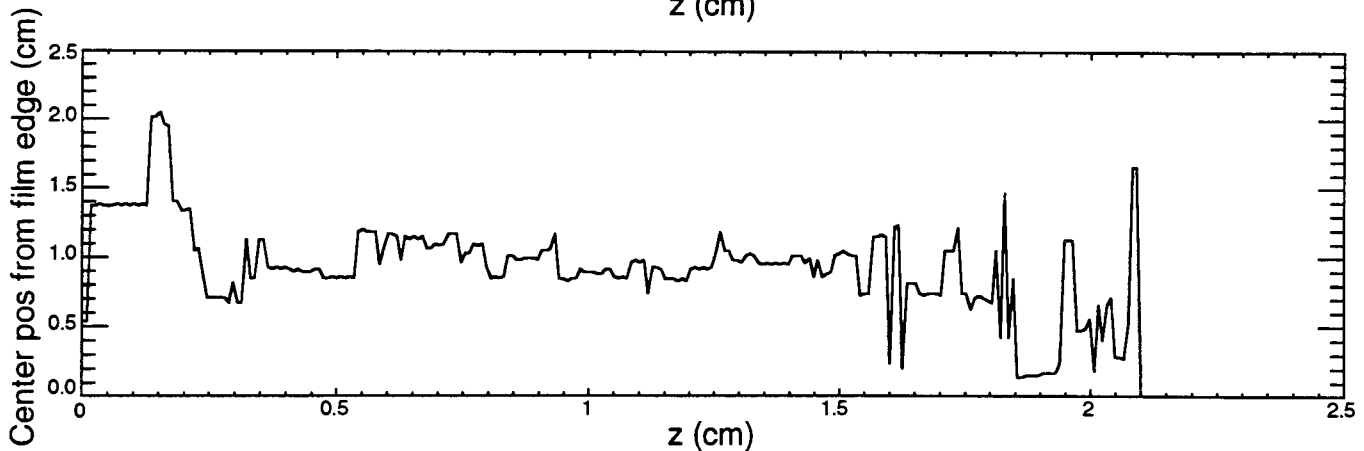
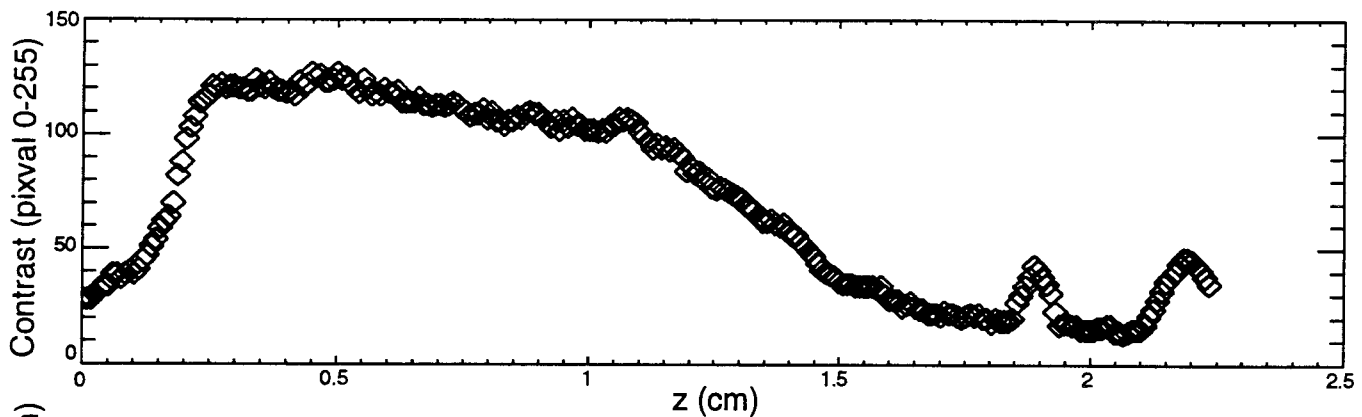
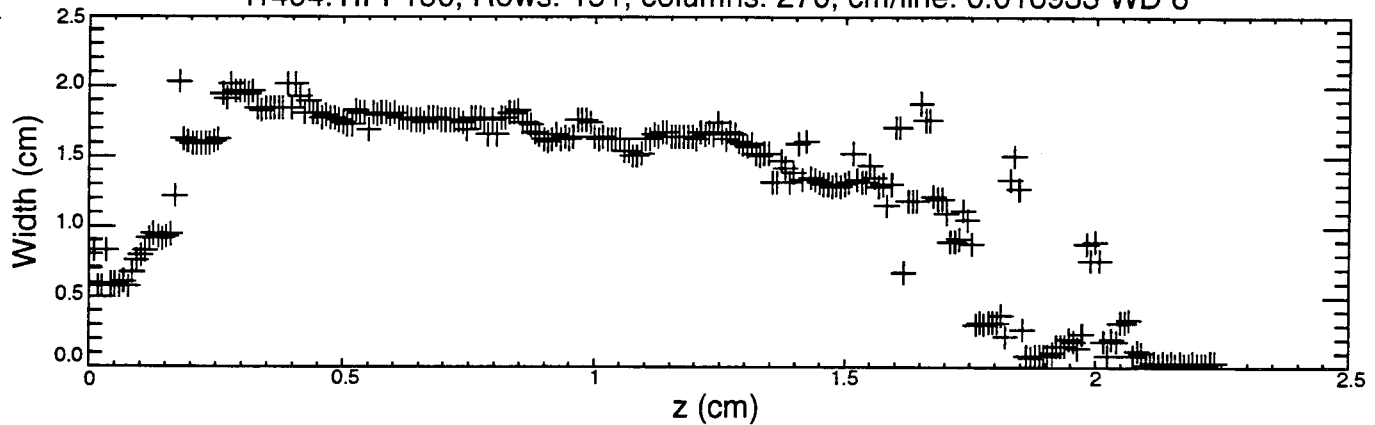
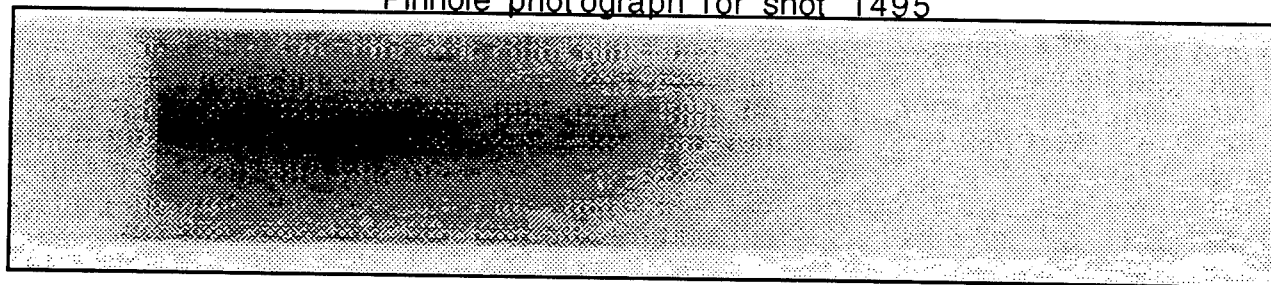


Figure 8c. Pinhole photograph and analysis for shot 1494. Low contrast favors computer determination of pinch radius. Shown, as a function of axial position z are 1) pinhole photograph; 2) pinch diameter, determined as described in the text; 3) image contrast (maximum 255); 4) position of darkest point ("center" of pinch). The overall pinch width was taken to be the average of the values in (2), except that points were not included when contrast was less than 50. The center-point position gives some indication of the straightness of the pinch.

Pinhole photograph for shot 1495



i1495.TIFF150; Rows: 151, columns: 270; cm/line: 0.016933 WD 6

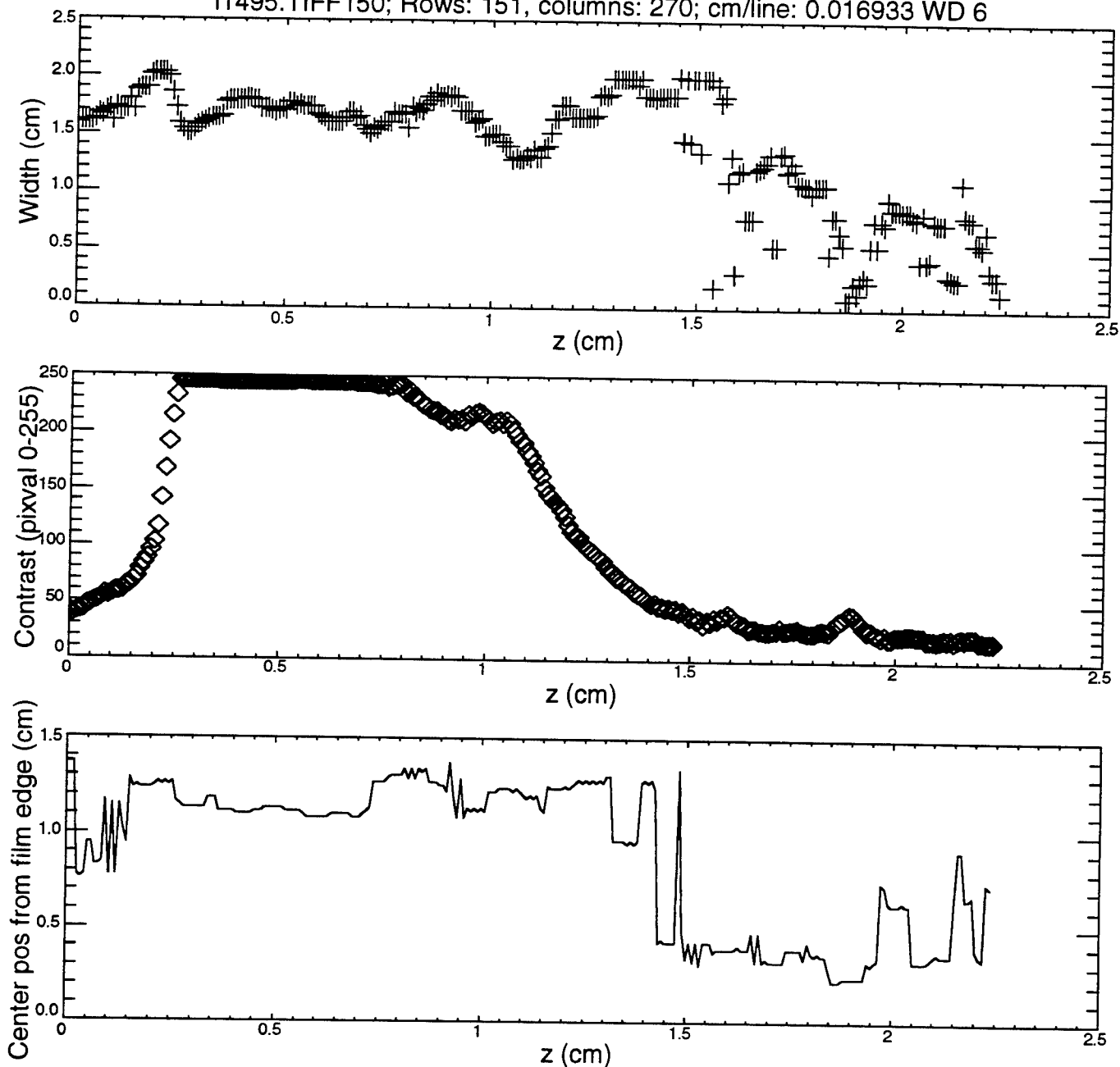
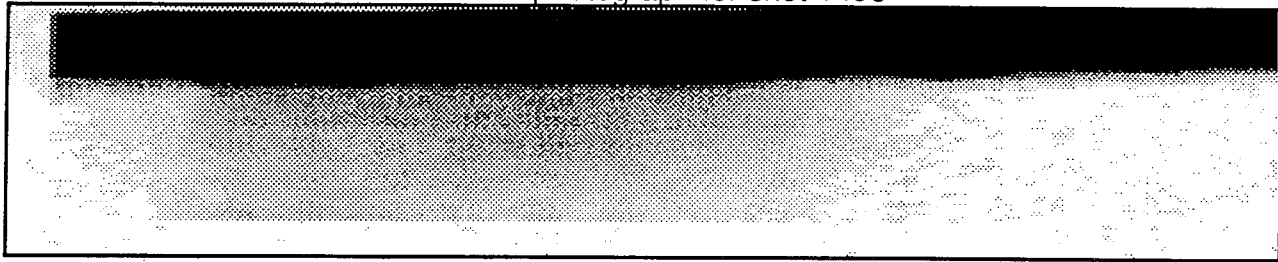


Figure 8d. Pinhole photograph and analysis for shot 1495. Shown, as a function of axial position z are 1) pinhole photograph; 2) pinch diameter, determined as described in the text; 3) image contrast (maximum 255); 4) position of darkest point ("center" of pinch). The overall pinch width was taken to be the average of the values in (2), except that points were not included when contrast was less than 50. The center-point position gives some indication of the straightness of the pinch.

Pinhole photograph for shot 1496



i1496.TIFF150; Rows: 151, columns: 270; cm/line: 0.016933 WD 6

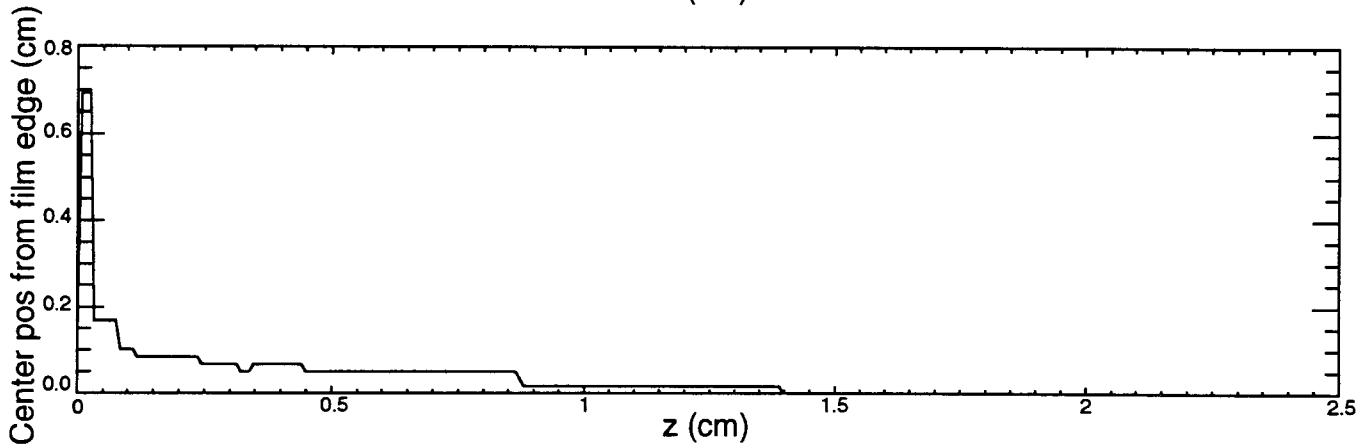
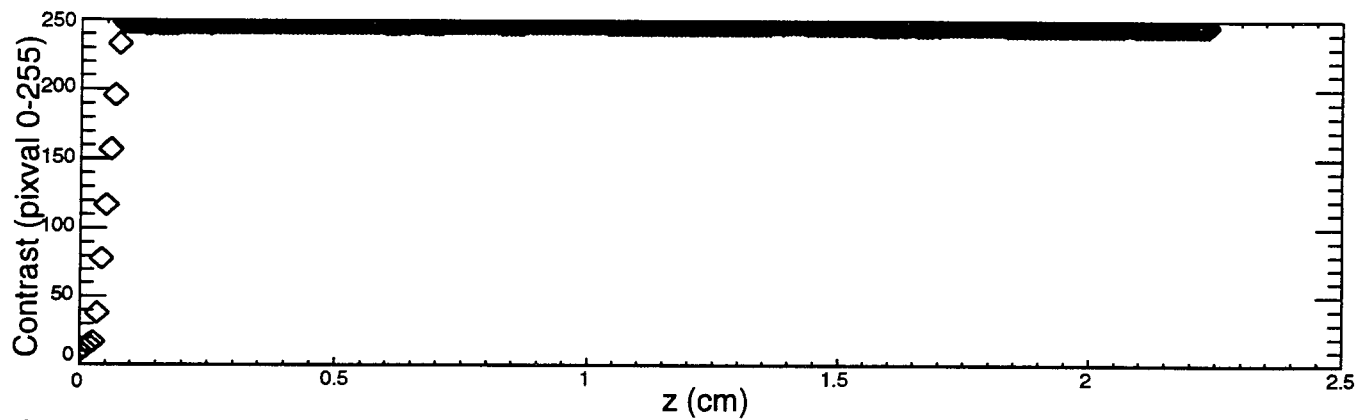
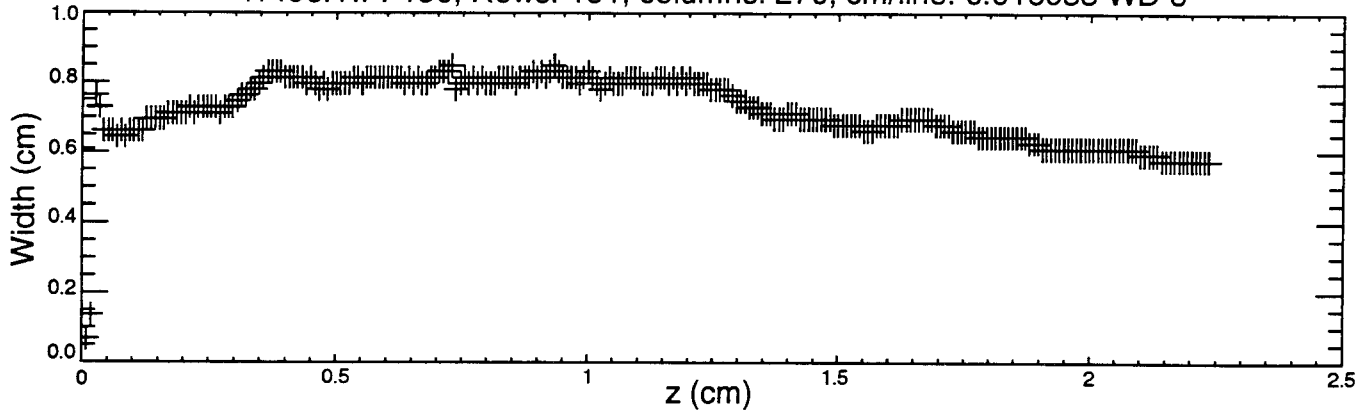


Figure 8e. Pinhole photograph and analysis for shot 1496. This photograph was obviously ruined by light leakage on the top ($r=0$). Shown, as a function of axial position z are 1) pinhole photograph; 2) pinch diameter, determined as described in the text; 3) image contrast (maximum 255); 4) position of darkest point ("center" of pinch).

Pinhole photograph for shot 1497

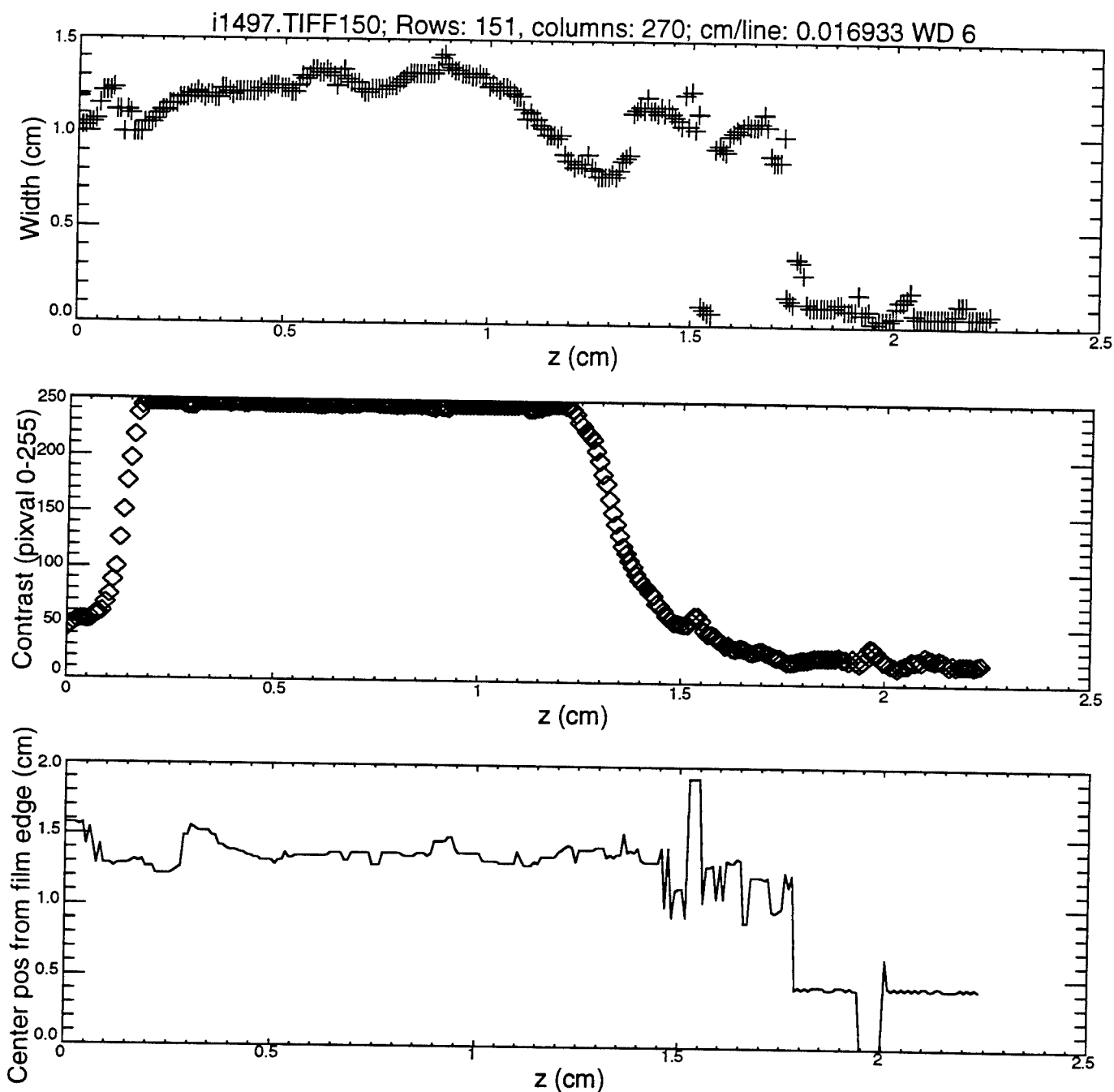
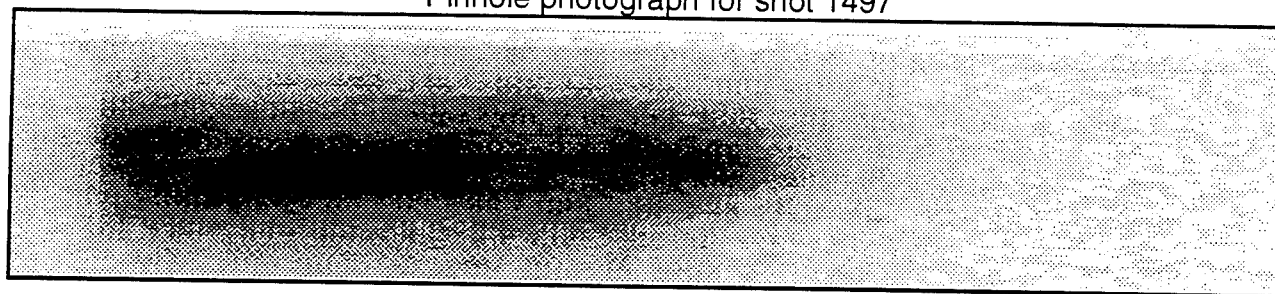


Figure 8f. Pinhole photograph and analysis for shot 1497. Shown, as a function of axial position z are 1) pinhole photograph; 2) pinch diameter, determined as described in the text; 3) image contrast (maximum 255); 4) position of darkest point ("center" of pinch). The overall pinch width was taken to be the average of the values in (2), except that points were not included when contrast was less than 50. The center-point position gives some indication of the straightness of the pinch.

Radius of radiating region

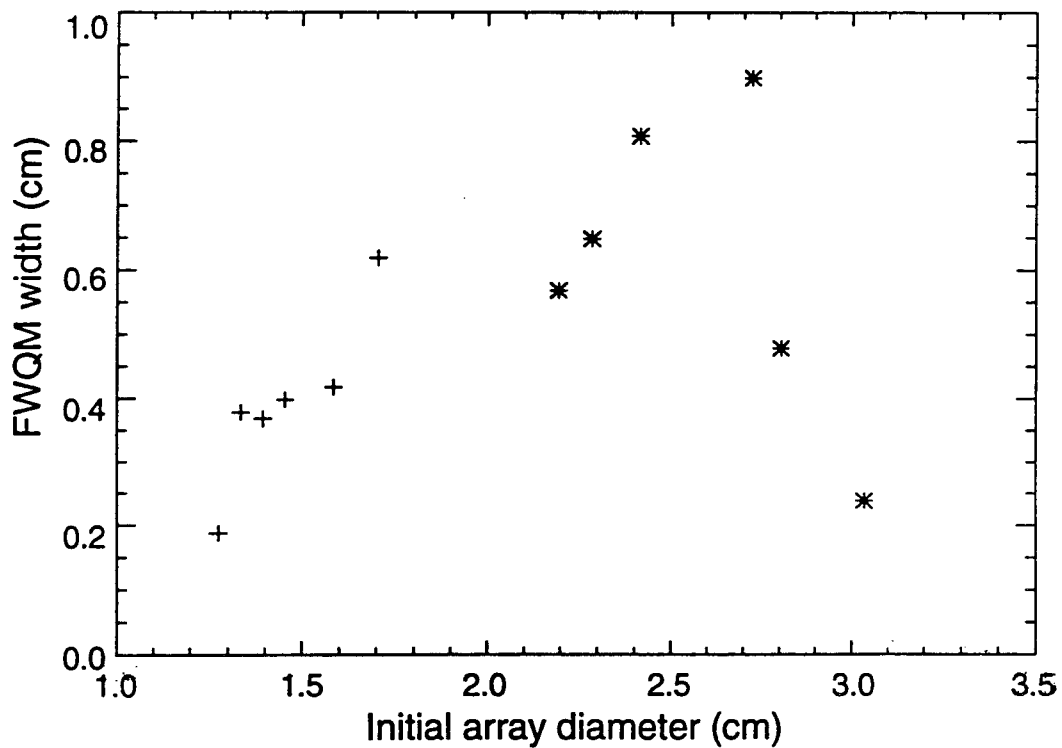
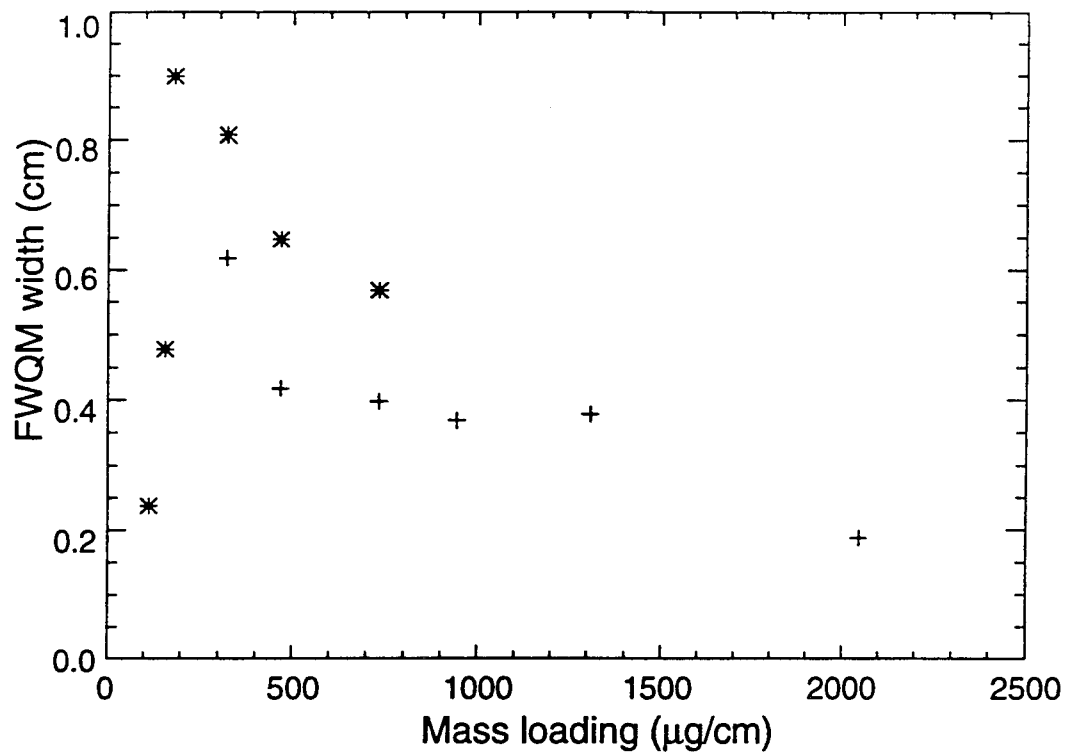


Figure 9. Results of the pinhole photograph analysis. The measured radius of the radiating region (by the FWQM method), plotted as a function of array linear mass density and of initial array radius. Measurements from set 1 are plotted with a plus (+), while those from set 2 are plotted with a star (*).

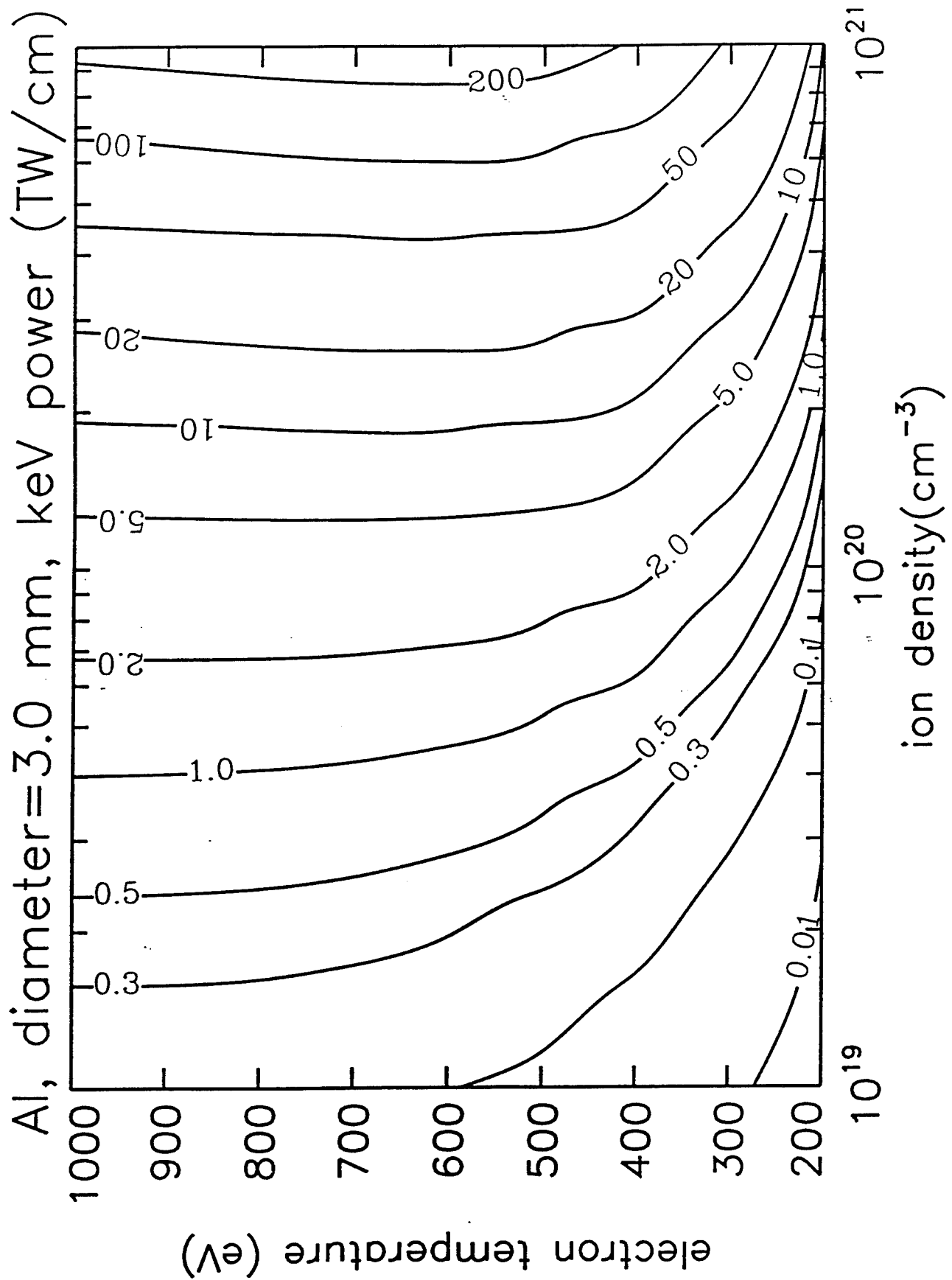


Figure 10. Results of CRE theoretical calculations showing the values of electron temperature and ion density that would generate various values of keV radiative power, for a pinch of radiating diameter 3 mm (e.g., shot 1483).

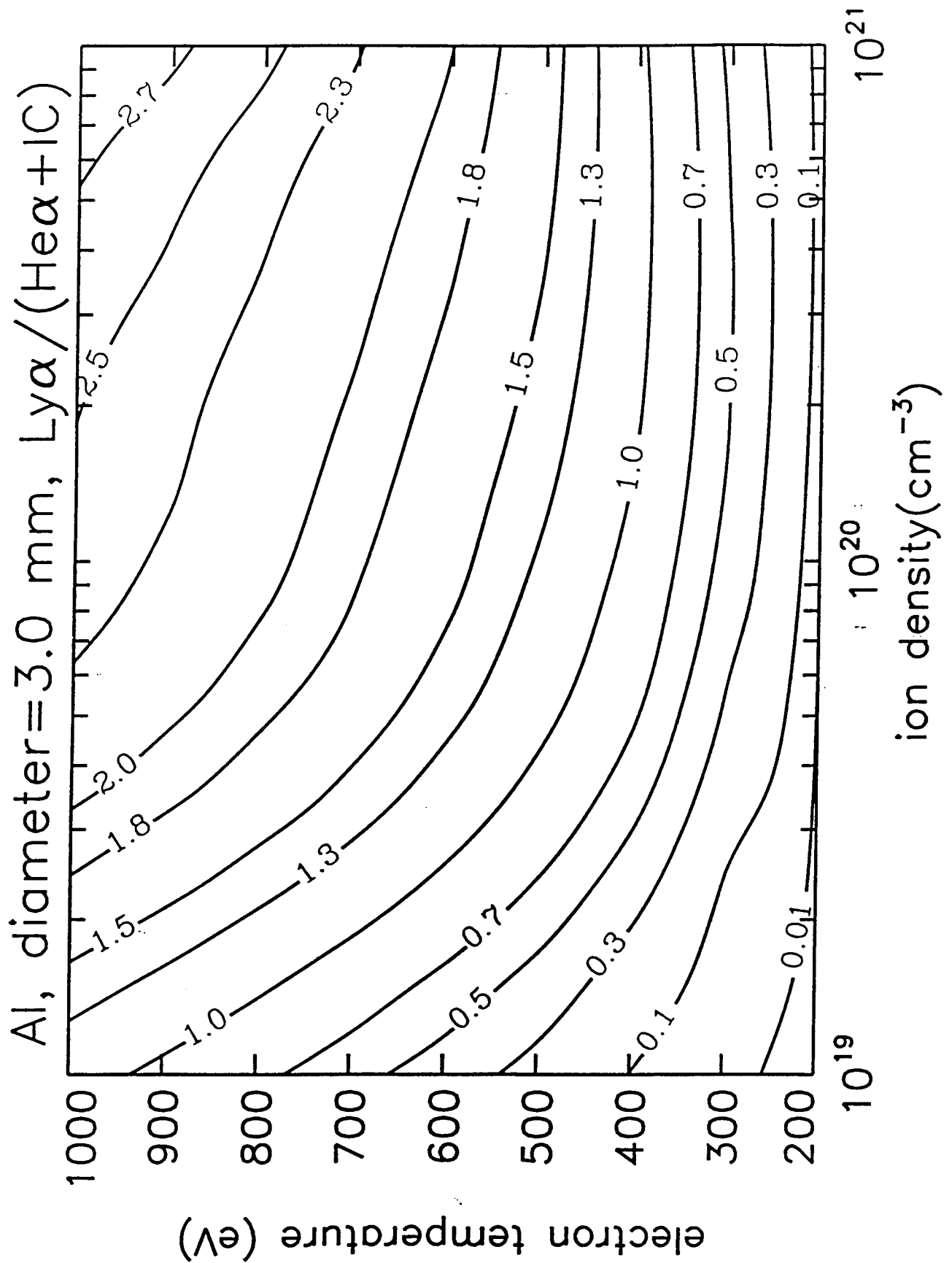


Figure 11. Results of CRE theoretical calculations showing the values of electron temperature and ion density that would generate various values of the Ly α to He α line ratio, for a pinch of radiating diameter 3 mm (e.g., shot 1483). For these contours, the He α line strength includes the intercombination line.

keV Power

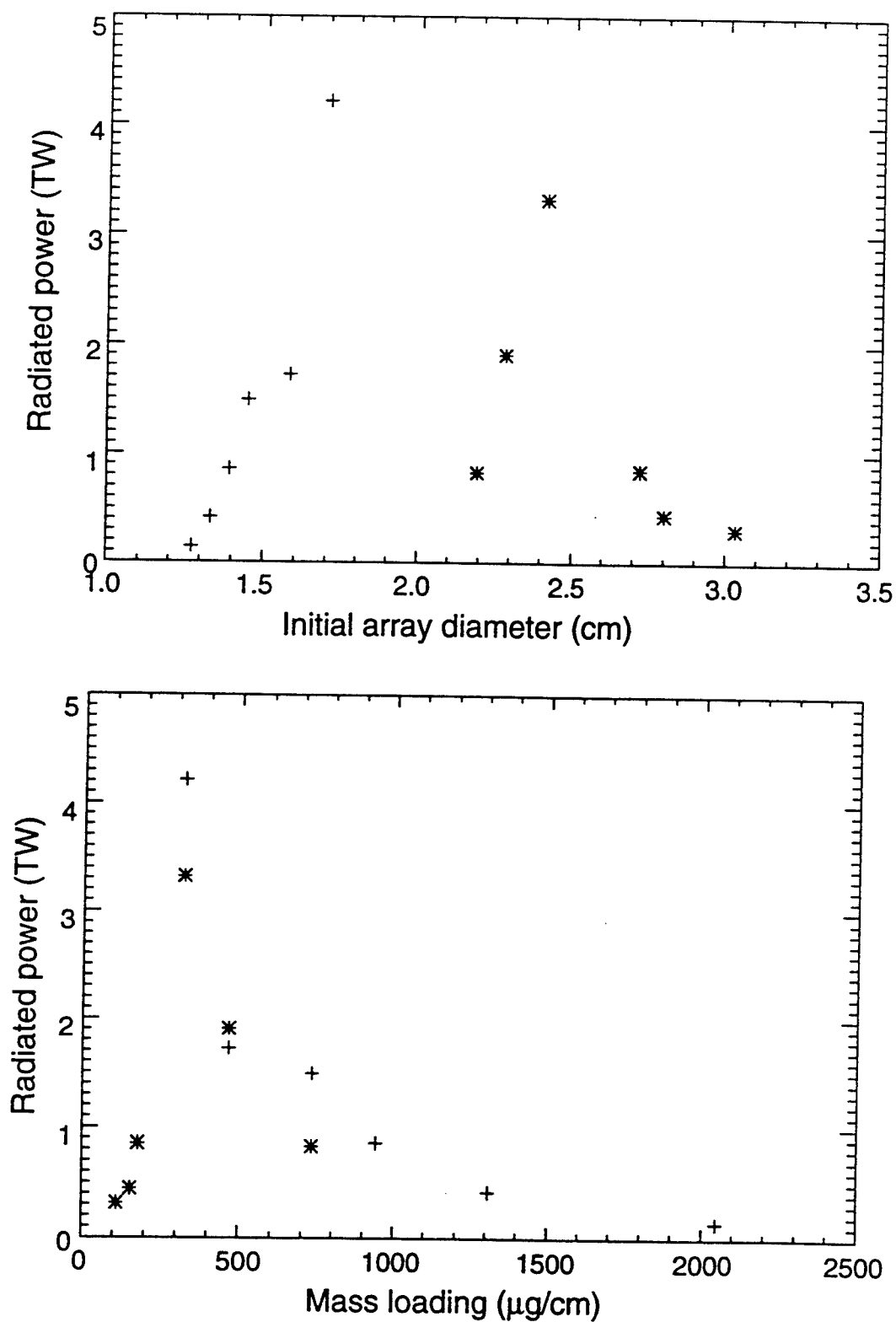


Figure 12. The keV radiative power as a function of both array linear mass density and of initial array radius. Measurements from set 1 are plotted with a plus (+), while those from set 2 are plotted with a star (*).

Ion density

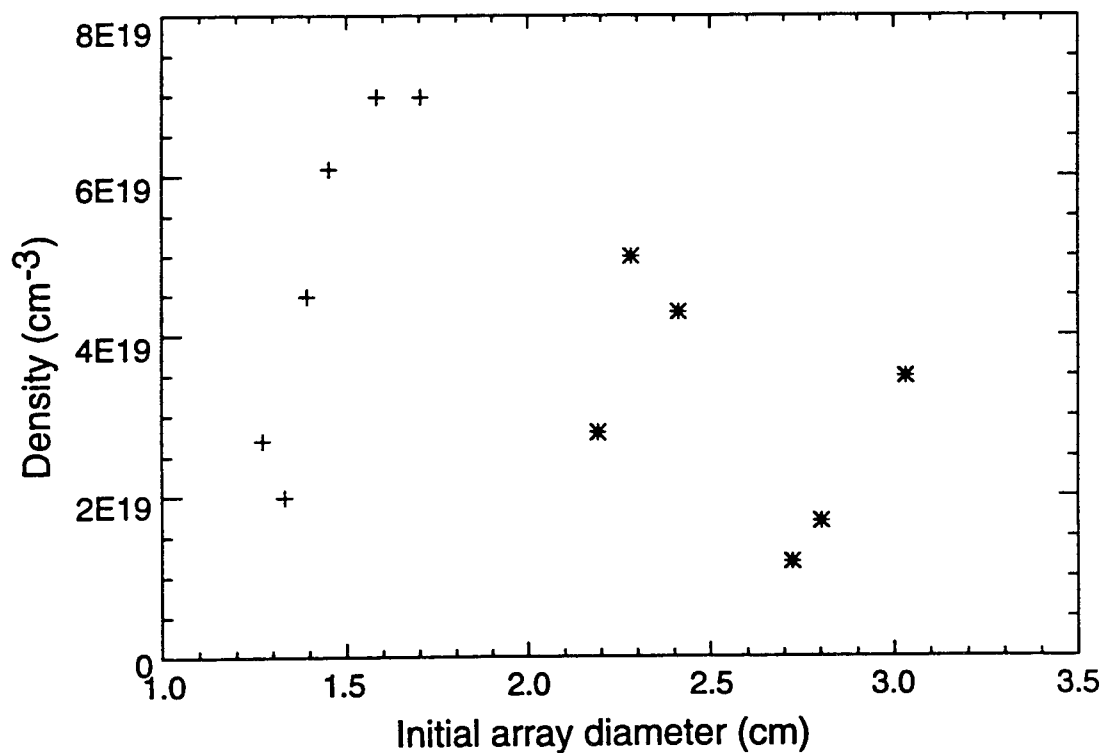
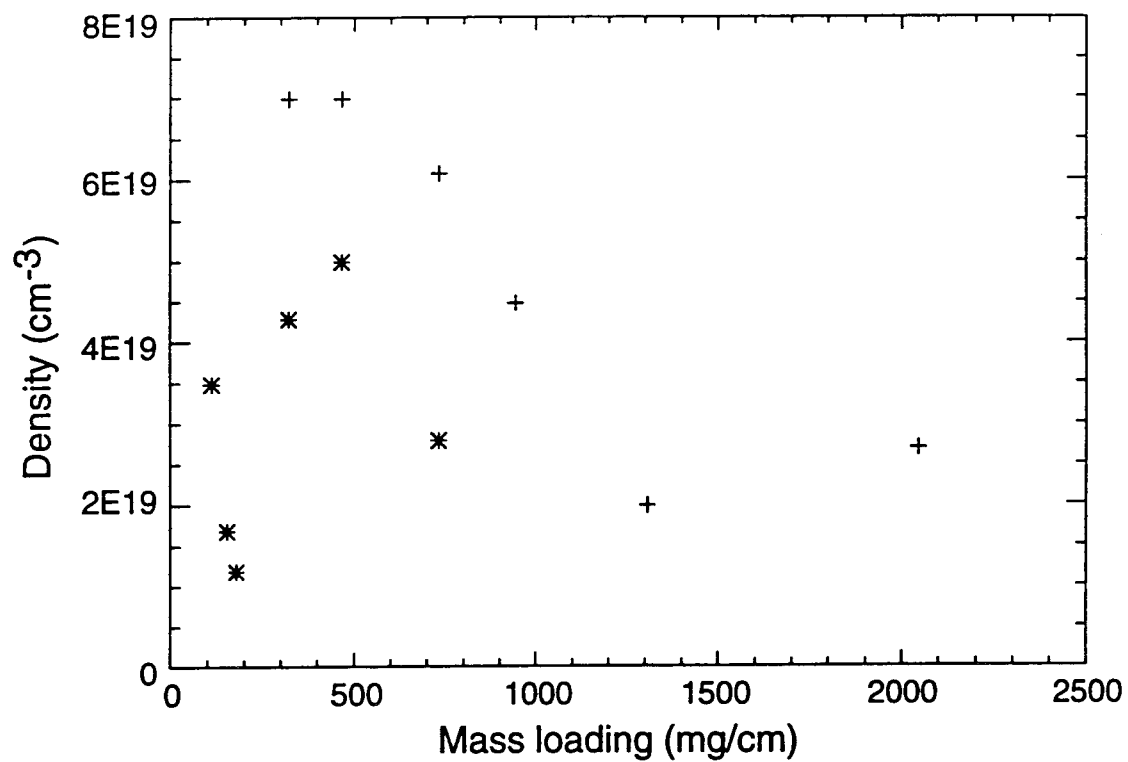


Figure 13. Ion density, inferred from the spectroscopic, pulsewidth and pinhole measurements, plotted as a function of both array linear mass density and of initial array radius. Measurements from set 1 are plotted with a plus (+), while those from set 2 are plotted with a star (*).

Electron temperature

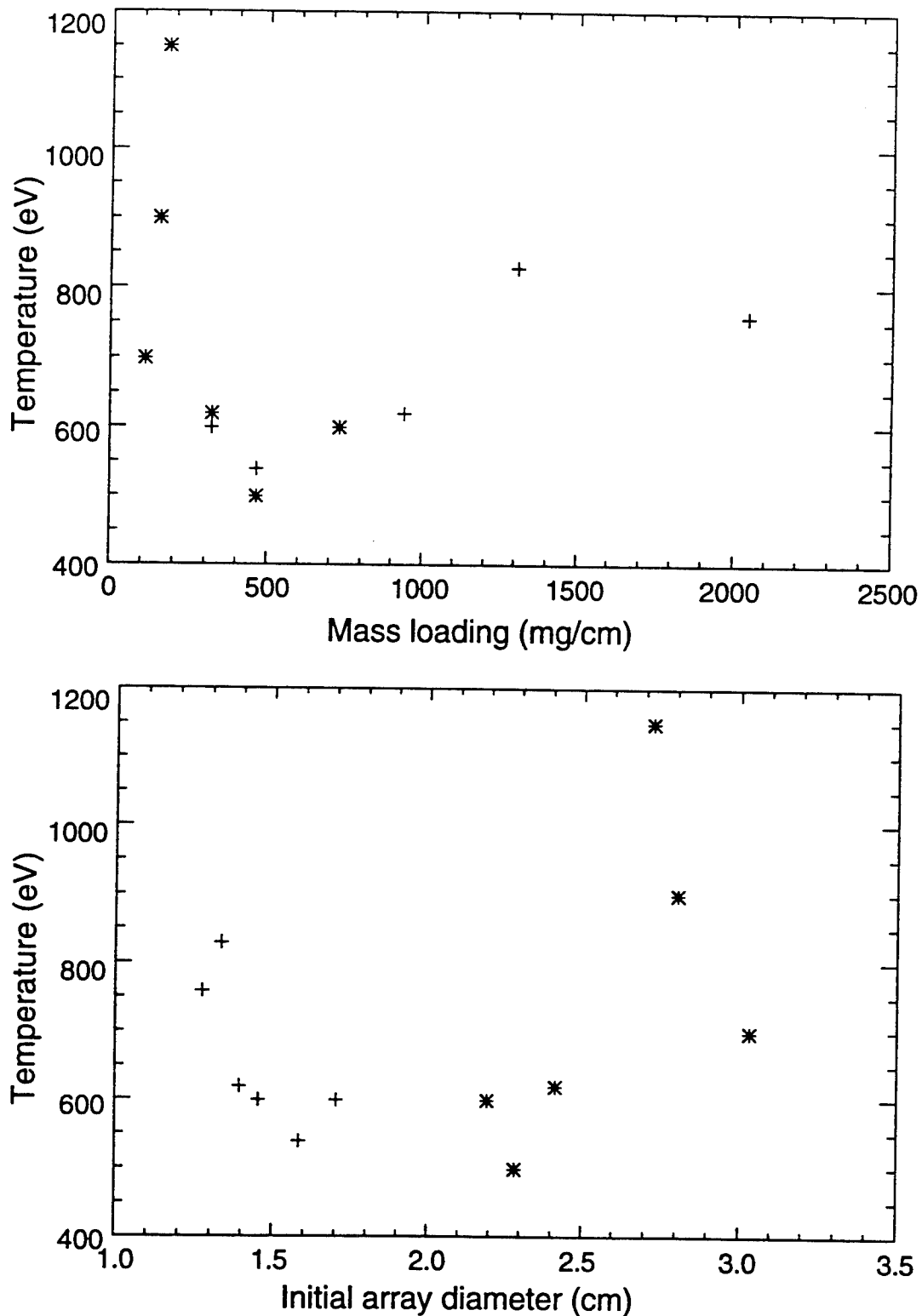


Figure 14. Electron temperature, inferred from the spectroscopic, pulsewidth and pinhole measurements, plotted as a function of both array linear mass density and of initial array radius. Measurements from set 1 are plotted with a plus (+), while those from set 2 are plotted with a star (*).

K-shell radiating mass fraction

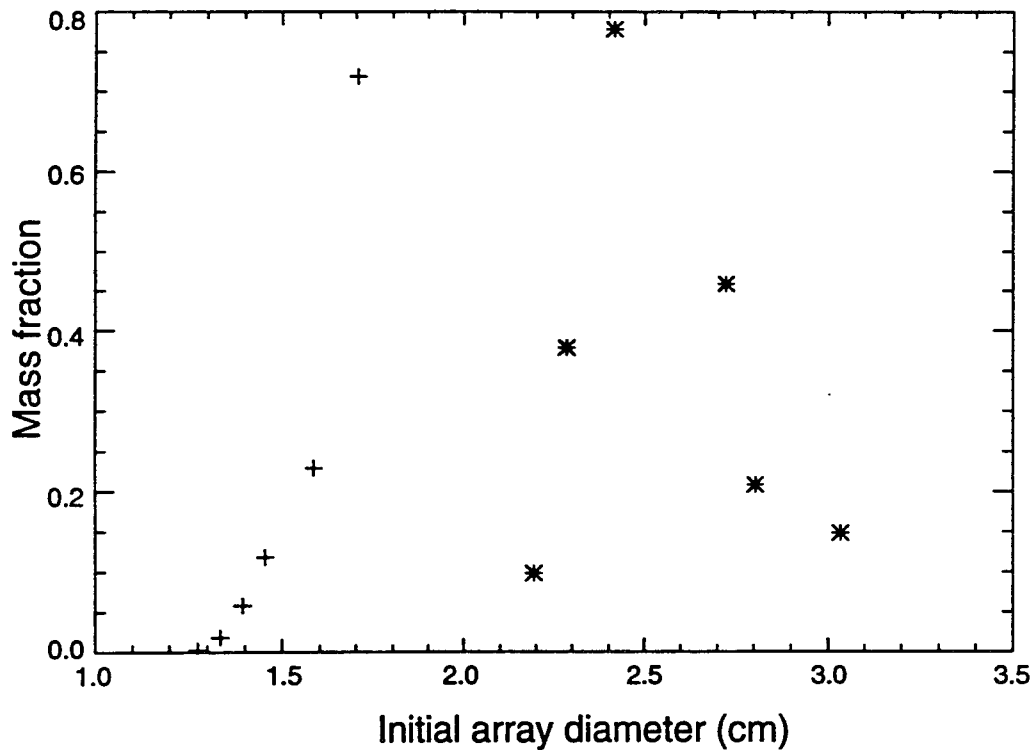
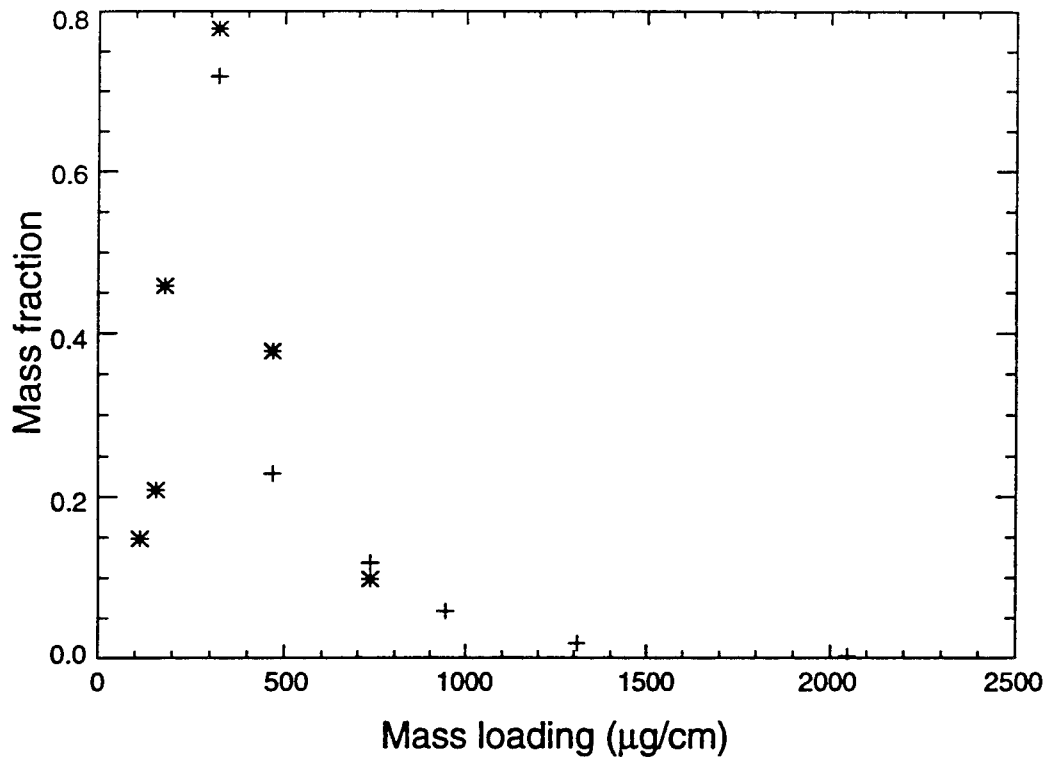


Figure 15. Fraction of the total imploding mass that is located in the radiating region. Computed from the measured pinch radius, the inferred ion density, and the known wire array mass. The mass fraction is plotted as a function of both the initial linear mass density of the array and of initial array radius. Measurements from set 1 are plotted with a plus (+), while those from set 2 are plotted with a star (*).

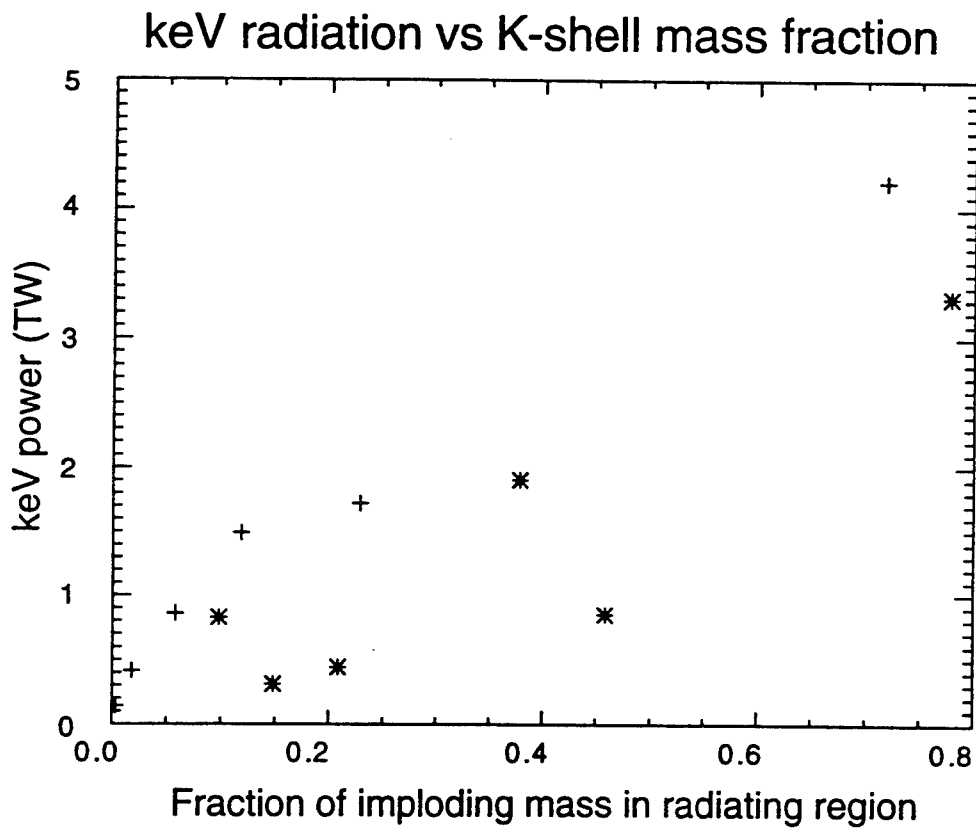
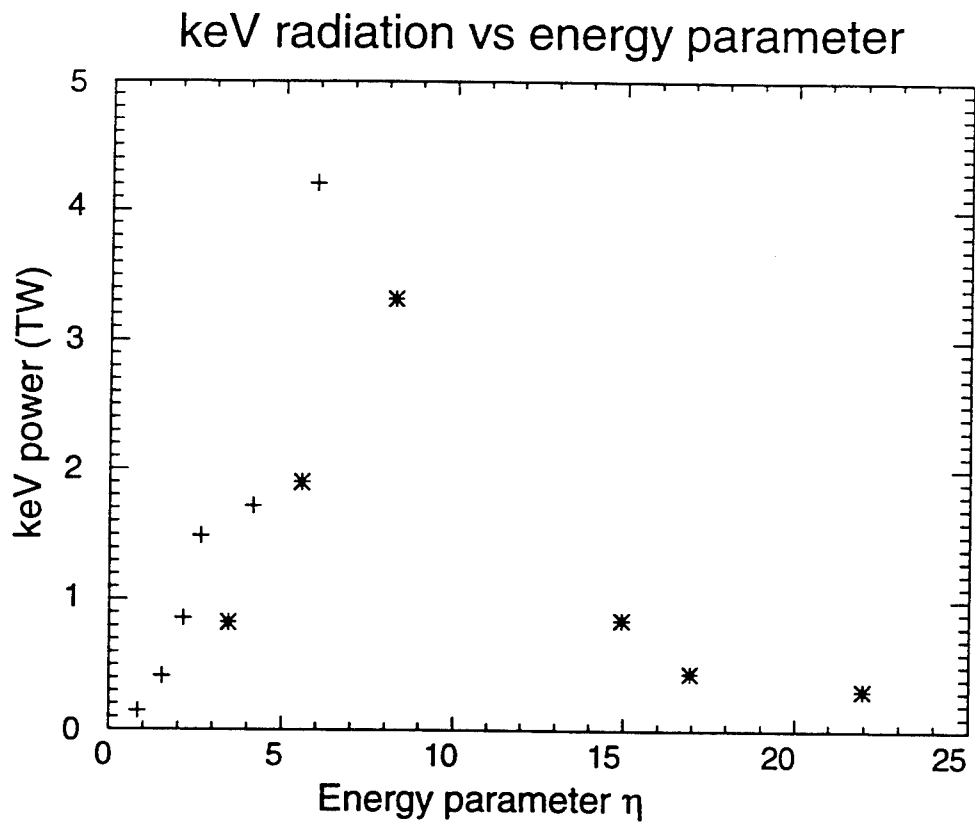


Figure 16. The keV radiative power, as a function of both the parameter η , which indicates the average kinetic energy per particle at stagnation; and of the fraction of total mass in the radiating region (plotted in Fig. (15)). Measurements from set 1 are plotted with a plus (+), while those from set 2 are plotted with a star (*).